Electrochemical H Insertion in Pd Thin Films

by

David Y. Young

S.B., Materials Science and Engineering / Electrical Engineering
Massachusetts Institute of Technology (2012)

Submitted to the Department of Materials Science and Engineering
in Partial Fulfillment of the Requirements for the Degree

of

Master of Science in Materials Science and Engineering
at the
Massachusetts Institute of Technology

June 2018

Signature redacted

Signature of Author............

....
Department of Materials Science and Engineering
Signature redacted May 9, 2018

Certified by...

....
Yet-Ming Chiang
Kyocera Professor, Materials Science and Engineering
Signature redacted Thesis Supervisor

Accepted by..

....
Donald R. Sadoway
John F. Elliott Professor of Materials Chemistry, Materials Science and Engineering
Chair, Department Committee on Graduate Studies

1
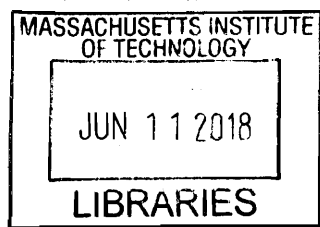
Electrochemical H Insertion in Pd Thin Films

by

David Y. Young

Submitted to the Department of Materials Science and Engineering

on May 9, 2018 in Partial Fulfillment of the

Requirements for the Degree of Master of Science in

Materials Science and Engineering

ABSTRACT

Metal hydrides are pertinent to several applications, including hydrogen storage, gas separation, and electrocatalysis. The Pd-H system is used as a model for metal-hydrogen systems and the effect H insertion has on their properties. A study was conducted to assess the performance of various electrochemical cell formats in electrochemically inserting H into Pd, which is important in building devices for the above applications. A set of *in situ* X-ray diffraction apparatuses were built to enable simultaneous electrochemical H insertion and measurement of PdH_x composition. A comparison between aqueous and solid electrolytes, temperature, and thin film vs. bulk Pd revealed that thinner films, lower temperatures, and aqueous electrolytes tended to promote higher achievable H content, with the highest H:Pd ratio observed being 0.96 ± 0.02. These results not only show high H loading into Pd but also both reproducibility and a clear association between varied parameters and cell performance.

In addition, the stability and performance of high temperature solid oxide electrolytes was investigated. A novel *in situ* calorimeter was constructed to enable the study of high temperature solid oxide electrolyte degradation while under operating conditions, similar to recent work in calorimetric analysis of battery stability. This calorimeter has a power detection sensitivity of 16.1 ± 11.7 mW, which is sufficient for detecting and quantifying many of the degradation and other side reactions that occur during high temperature operation of a solid oxide electrolyte in an electrochemical cell. This apparatus provides a tool needed to assess stability and life of solid oxide electrolytes under operation, a critical component to developing higher performing solid oxide electrochemical devices.

Thesis Supervisor: Yet-Ming Chiang

Title: Kyocera Professor, Materials Science and Engineering

Table of Contents

I.   Introduction and background

Metal-hydrogen systems have been studied for a variety of applications dating back as early as the 1860s [1]. In particular, the Pd-H system has been widely used as a model metal hydride to investigate the interactions between H and its metal host and the resulting changes in material properties. PdH_x has been studied in the context of hydrogen storage [2-5], in which various methods are used to increase the amount of H absorbed by Pd or change the rates of H uptake and release. Work in this area is becoming increasingly important from the standpoint of developing a hydrogen energy economy, in which H is used as a primary source of fuel. Hydrogen storage materials require high H storage density, which metal hydrides do provide, but further research into both the stability and kinetics of these systems during operation is needed [6]. Gas filtering and separation is another application that utilizes the selectivity of Pd for H compared to other gases [7-9]. Electrocatalysis [10-12], superconductivity [13-15], and mechanical damage caused by hydrogen embrittlement [16] are other areas of interest. In electrocatalysis applications, strain caused by inserted H in the Pd lattice can change the binding energies of adsorbed H intermediates pertinent to the activity of electrochemical reactions like the hydrogen evolution reaction (HER).

Several of these applications require H to be absorbed by Pd in large quantities, but loading H into Pd to high H concentrations (H:Pd ratio greater than 0.7) is non-trivial. One method is to simply change the partial pressure of H_2 gas in the environment. However, as shown in Figure 1, the relationship between PdH_x composition and H_2 pressure is logarithmic at higher loadings, so orders of magnitude pressure increase are necessary to substantially change composition. At 1 atm of H_2, the H:Pd ratio in PdH_x is about 0.7, but to achieve a H:Pd ratio close to 1, pressures on the level of 10,000 atm is needed. For applications that require high H loading, this pressure method is not practical, but the relationship between pressure and composition is well-documented for both the low H composition α phase and the high H composition β phase [17-19]. In addition, thermodynamic models have been proposed to relate the enthalpy, entropy, and composition of PdH_x to an equivalent fugacity of H_2 [20].
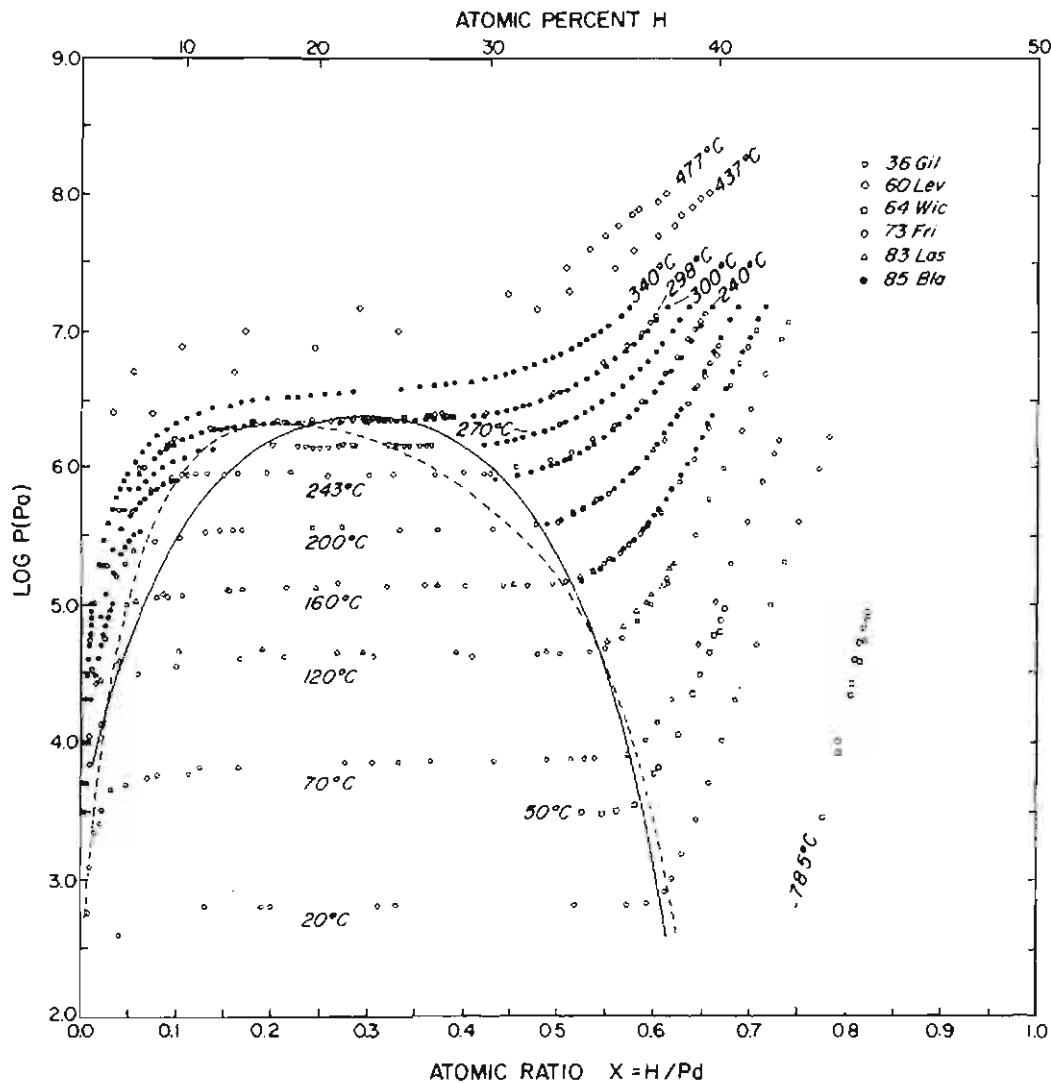
4

Figure 1. Pressure vs. composition of the Pd-H system for several isotherms. The phase left of the miscibility gap is known as α-Pd, while the phase to the right is called β-PdH$_x$. Reproduced with permission from [21].

As an alternative to pressure, electrochemistry can be used to increase the composition of PdH$_x$. The inherent advantage of this method is that it enables much higher H:Pd ratios at ambient pressure and temperature. By applying a potential bias to Pd in an electrochemical cell, H$^+$ is driven to the surface of the electrode-electrolyte interface, where it combines with an e$^-$ to form a surface-adsorbed H intermediate. This H can then diffuse into Pd or combine with another surface H atom to form H$_2$ gas. These two reaction paths compete with each other, the former

5

known as the H insertion reaction and the latter called HER. In addition, because the H inserted into Pd is at a higher energy state compared to the H in the surround gas environment, H will desorb from the Pd lattice and return to the surrounding environment as H_2 gas. The opposite process occurs if H is extracted from the Pd lattice through the reverse electrochemical process to below the equilibrium concentration. A diagram of all three of these processes in the forward and reverse direction (H insertion/extraction, HER or H oxidation reaction (HOR), and H absorption/desorption) is described in Figure 2.
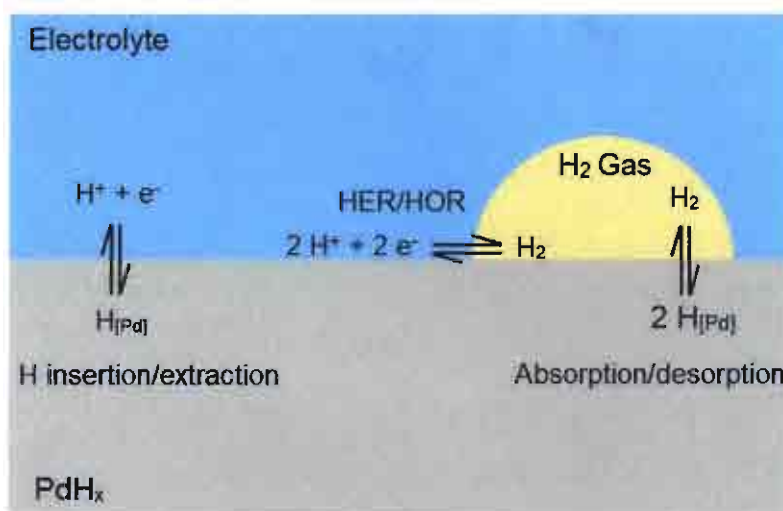

Figure 2. Chemical processes occurring at the PdH_x electrode-electrolyte interface of an electrochemical cell during application of electrochemistry. Under a reductive potential and current, H^+ in the electrolyte can recombine with electrons to form H that is either inserted into the PdH_x electrode or evolved as H_2 gas (HER). The reverse processes of H extraction and H oxidation (HOR) occur under an oxidative potential. In addition, an exchange between H in PdH_x and H in H_2 gas is made through an absorption/desorption reaction that seeks to equilibrate the energy state of H in both phases.

Electrochemistry provides a useful tool for loading H into Pd near ambient conditions, but the relationship between electrochemical inputs and PdH_x composition are not well-defined for different electrochemical conditions. Furthermore, methods for measuring PdH_x composition during application of electrochemistry are not straightforward, and many of these methods create

significant errors and biases that convolute results. An assessment of these different measurement techniques is made here, and *in situ* X-ray diffraction (XRD) is chosen as the most accurate and reliable for reasons detailed below.

With measurement tools in hand, an investigation of different electrochemical cell formats can be conducted. Classic aqueous architectures, in which Pd is placed in an acidic aqueous electrolyte, are considered, while solid-state cells utilizing solid oxide and polymer electrolyte membrane fuel cell technologies are also studied [22-24]. On paper, solid-state electrolytes provide several advantages over aqueous cells: (1) higher potential window unrestricted by the aqueous media, (2) larger active temperature range than water, and (3) less interruption of the electrode-electrolyte interface from bubbles. However, they require thin film, rather than bulk, Pd to be used. These electrochemical cells are fabricated and contrasted to demonstrate the effect that different cell architectures and operating conditions have on H insertion in Pd.

The goals of this study are threefold: (1) create an accurate and reliable method for measuring PdH_x composition during application of electrochemistry, (2) develop and assess an array of electrochemical cells operating under different conditions, and (3) understand the factors the promote or inhibit higher compositions of PdH_x. Herein, a set of tools and apparatuses constructed for simultaneous electrochemistry and composition measurement are described, and a comparison between aqueous and solid electrolytes, temperature, and thin film vs. bulk Pd is made with respect to their effect on attainable PdH_x composition. Finally, the stability and performance of high temperature solid oxide electrolytes for use in this application and others is investigated.

II.   Measurement of electrochemical H loading in Pd

A. An assessment of the available measurement techniques

The measurements techniques used to quantify the amount of H in these PdH_x compounds created using electrochemistry generally fall into two categories: (1) *ex situ* measurement of H leaving PdH_x after electrochemical loading is complete and (2) *in situ* measurement of some changing property of PdH_x as loading is occurring. The first category has an inherent disadvantage in that these methods do not allow time-resolved measurements of composition

7

during a H loading experiment. Instead, the measurement only captures the final H content at the end of the experiment. Included in this category are outgassing and coulometry. The former involves placing the PdH_x sample in a sealed chamber and degassing it using a combination of time and temperature [18, 19, 25]. The escaping H_2 gas can be quantified using gas displacement, monitoring pressure changes, or mass spectrometry. An additional disadvantage for this method is the loss of H between when the loading experiment is performed and when the outgassing begins, especially if the PdH_x sample needs to be relocated to a different chamber or vessel.

Using coulometry to measure H content involves applying an oxidative potential to the PdH_x electrode and essentially counting the H atoms leaving in the form of H^+ and e^- [26]. This method can typically be done in the same cell as during H loading. However, there is typically a small time lag between when potential and current for loading are applied and when the reverse potential and current are switched on for coulometric measurements. Even if the time lag is small (on the order of ms), it may be enough for a substantial amount of H to desorb from the PdH_x electrode and escape. Furthermore, if any residual H_2 gas remains on the surface of the electrode from the loading experiment, the applied potentials will oxidize that gas as well, resulting in an overestimation of the amount of H present.

One proposed method that sits on the line between *ex situ* and *in situ* is measurement of the open circuit voltage (OCV) of PdH_x. During electrochemistry, the electrochemical driving force is temporarily removed, and the OCV is measured. In principle, this OCV can be correlated to the H concentration in Pd using a set of thermodynamic relationships. However, this method requires that electrochemistry be paused briefly, so H can leak out during the measurement. In this study, the OCV technique was initially attempted, but convoluting factors such as ohmic relaxation and uneven H distribution created inconsistent and unreliable results.

There are three primary ways to measure H content *in situ* that removes the issue of time resolution and potential loss of H between loading and measurement of loading. The first is measuring the change in mass of the PdH_x electrode. This method is commonly employed with a quartz crystal microbalance (QCM) that indirectly measures mass change by resonant frequency shifts of the quartz crystal [27]. The downsides of using QCMs are that the Pd must be deposited onto the QCM in thin film form and that strain from the lattice expansion of Pd when H is

inserted causes frequency shifts as well. These strain-induced frequency shifts require nontrivial corrections be made to the result and have to be calibrated using a separate loading measurement technique.

Another *in situ* technique makes use of resistance changes in the PdH$_x$ electrode compared to pure Pd, known as the resistance ratio method [28]. An empirical relationship has been developed between the change in resistance of PdH$_x$ as composition changes (Figure 3). Though this technique allows for fairly facile measurements of PdH$_x$ composition during electrochemical loading experiments, it nevertheless presents a plethora of convoluting biases or errors, described in detail by Zhang et al. [28]. One glaring issue is the fact that there are two compositions possible for each resistance ratio, which creates ambiguity in the measured result. Furthermore, resistance changes in the sample could be due to other factors such as temperature, sample degradation or shunting through the electrolyte.
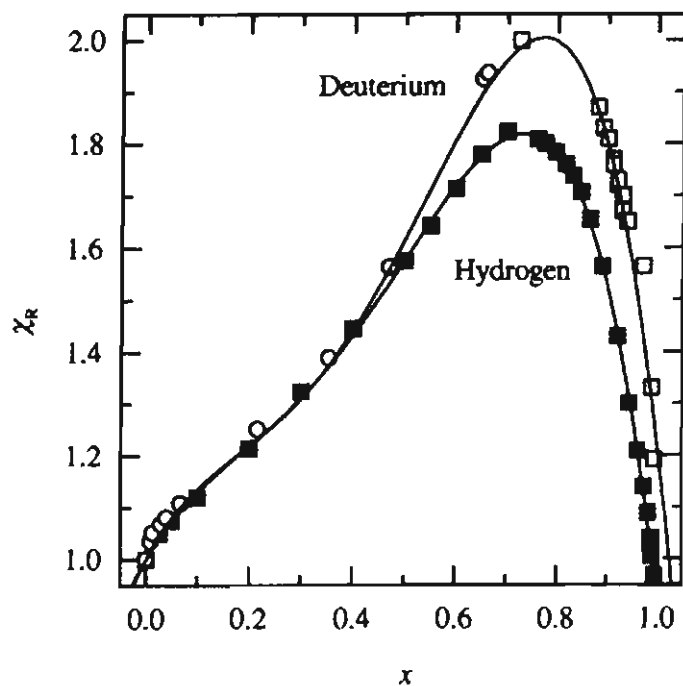

Figure 3. Resistance ratio (χ_R) vs. H:Pd or D:Pd ratio (x) for PdH$_x$ or PdD$_x$ compounds. Lines represent fits to the data with a fourth order polynomial. Reproduced with permission from [28].

Last but not least, *in situ* XRD is a method that directly measures the structural changes in PdH$_x$ as H is inserted. This technique, along with the closely related extended X-ray absorption fine structure (EXAFS), can be used to monitor changes in the lattice parameter of PdH$_x$, which expands during H insertion in a predictable and reproducible manner. Some convoluting factors, such as strain effects from the substrate in thin films or grain size effects, are present but are considered relatively minor. More importantly, traditional *in situ* XRD studies have required the use of synchrotron facilities, which prevent higher throughput given the limited availability of instrumentation and the requirements needed to set up experiments. Previous works utilizing *in situ* XRD [29-32] and EXAFS [33] have all used synchrotrons to provide an X-ray source. *In situ* XRD is the technique of choice for this study with modifications made to provide higher throughput experimentation.

B. *In situ* XRD apparatuses compatible with a lab-scale, powder X-ray diffractometer

The *in situ* XRD apparatuses used here are designed and constructed to take diffraction measurements without the need for a synchrotron. One apparatus is built to handle solid-state electrochemical cells in a H$_2$ gas environment, while another is fabricated for compatibility with an aqueous environment. One critical design criterion is that these apparatuses needed to be able to allow X-rays originating from an X-ray source to pass through the apparatus to the sample and reflect off the sample to a detector (Figure 4). This process is dissimilar from many synchrotron setups, which often have higher energy X-rays that penetrate through the apparatus and the sample entirely to a detector located at the end of the straight X-ray beam path.
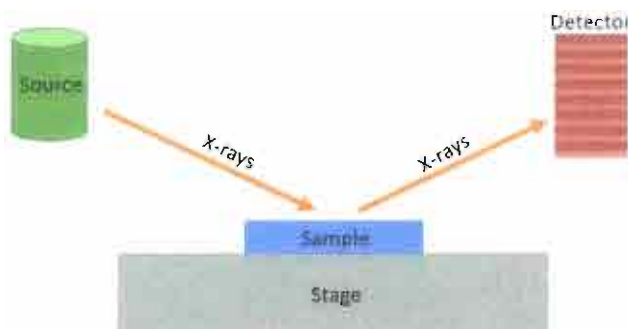

10

Figure 4. Diagram of an X-ray diffractometer setup for X-ray diffraction (XRD) measurements. X-rays emanate from an X-ray source and reflect off the sample before being collected by a detector.

The solid-state *in situ* XRD apparatus is designed to meet or exceed the criteria laid out in Table I. XRD for a range of $5° < 2\theta < 90°$ is necessary for full range scans of most relevant PdH_x and electrolyte peak positions. The apparatus needs to be gas tight for safety at high temperatures, during which the presence of high temperature H_2 gas can react with O_2 in the surrounding atmosphere if not sealed properly. Electrical requirements necessitate at least 5 feedthroughs, which includes 2 power feedthroughs attached to a heater coil and 3 electrical contacts to the electrochemical cell for 3-electrode measurements. Temperatures of at least 700 °C are desired stemming from the use of high temperature solid oxide electrolytes, which can typically operate in range between 300 and 1,000 °C.

Table I. Design criteria for solid-state *in situ* XRD apparatus.

Specification	Requirement
XRD	X-ray transparent windows for $5° < 2\theta < 90°$
Gas	Gas tight
Electrical	≥ 5 feedthroughs
Temperature	Up to 700 °C

Figure 5 shows the completed solid-state apparatus. A stainless steel frame bolted together with Cu gaskets ensures gas tightness for safe usage of H_2 gas at elevated temperatures. Two X-ray transparent Be windows are welded to either side of the frame, and a quartz optical window is positioned on top to enable *in situ* optical imaging. Gas and electrical feedthroughs bring gas environment control, electrochemistry, and heating capabilities. A heater control system (Omega) is hooked up to a transformer (Acme Electric) to allow to passage of 24 VAC to the heater coil. The inner wall of the apparatus is lined with fiberglass insulation, allowing the apparatus to reach a maximum temperature close to 800 °C. The electrochemical cell (described

11

in more detail in later sections) is secured with ceramic screws to a Macor ceramic block (Corning) that sits on top of a heating coil (Micropyretics Heaters International Inc.). Connections are made to the cell with either Pt wire or foil and are connected to a potentiostat (Bio-Logic). The entire apparatus is designed to fit snugly into a Smartlab X-ray diffractometer (Rigaku) and can operate in a range of $10° < 2\theta < 90°$.
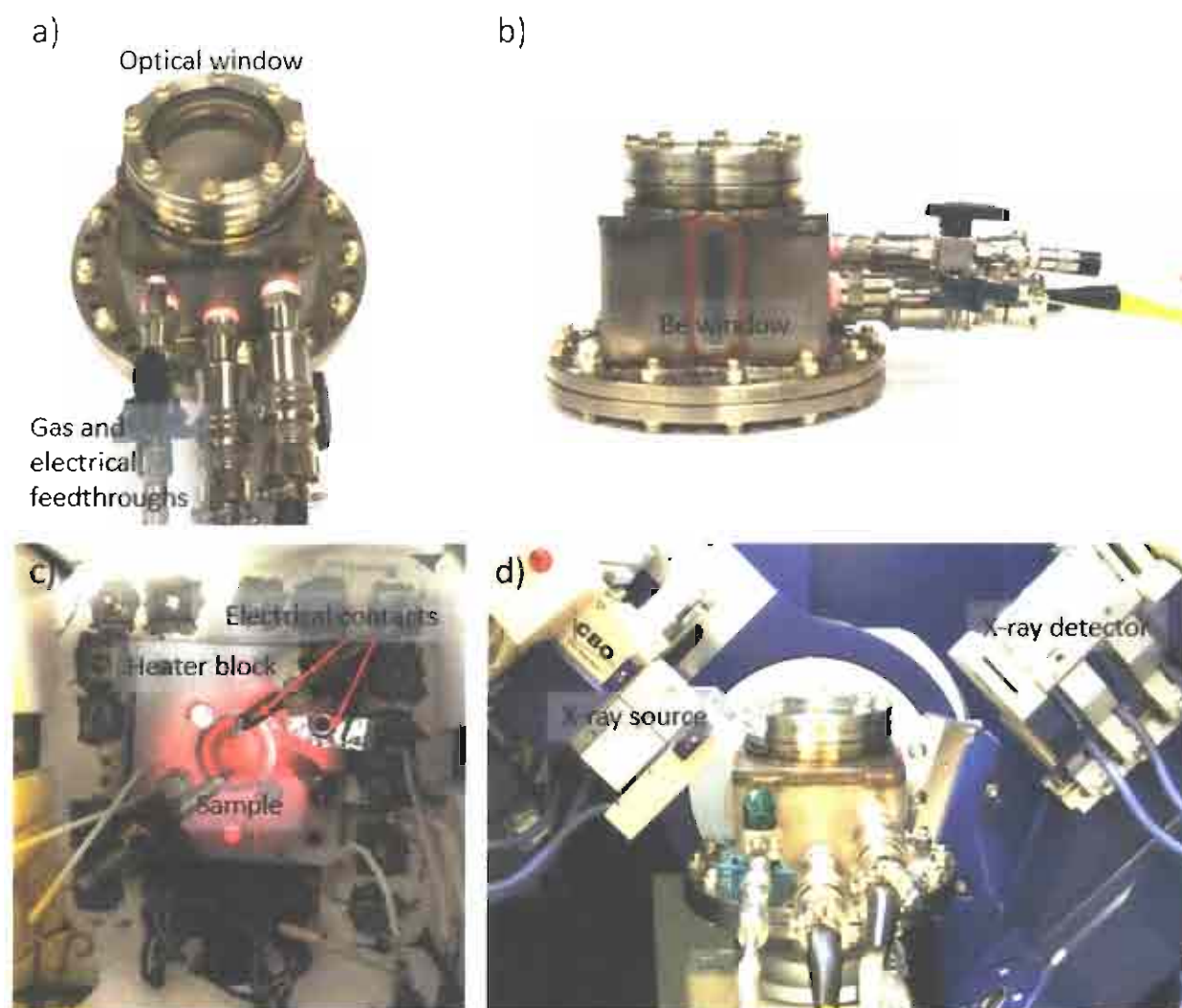

Figure 5. (a) Top view and (b) side view of the *in situ* XRD apparatus used for solid-state electrochemical cells showing stainless steel housing, an optical window for imaging, gas feedthroughs for flowing humidified H_2 and/or Ar gas, electrical feedthroughs for electrochemistry and heating, and X-ray transparent Be windows. (c) Internal view of the apparatus shows a heater block placed on top of a heater coil (not shown), an electrochemical

cell sample, and electrical contacts made to the electrodes of the sample. The internal elements are surrounded by fiberglass insulation. (d) The solid-state *in situ* XRD apparatus fits inside a Rigaku Smartlab X-ray diffractometer.

A separate apparatus is designed specifically for aqueous electrochemical cells with the criteria outlined in Table II. The apparatus requires similar XRD capabilities but fewer electrical feedthroughs due to not having the need for temperature control. Where aqueous electrolyte resides, the apparatus needs to be leak-proof. However, at the same time, venting is required for gas evolved during electrochemistry.

Table II. Design criteria for aqueous *in situ* XRD apparatus.

Specification	Requirement
XRD	X-ray transparent windows for $15° < 2\theta < 90°$
Liquid medium	Liquid tight
Electrical	≥ 3 feedthroughs
Gas	Gas venting

The completed aqueous *in situ* XRD apparatus is shown in Figure 6. The housing is 3D-printed from acrylonitrile butadiene styrene using a Mojo 3D printer (Stratasys). It is comprised of a well that can be filled with aqueous electrolyte as well as a vent for gas. Additionally, the top of the apparatus is sloped at 5° to allow gas bubbles that form during electrochemistry to travel towards the vent. X-ray transparent Kapton film is sealed over top with silicone. This Kapton film holds either a thin film or foil Pd cathode. An anode made from Pt foil is attached to a glass slide and inserted into the bottom of the well. Cu tape is used to make electrical contact to the Pd cathode. Ag/AgCl in saturated KCl is used as the reference electrode. It can be conveniently inserted into the well to make contact to the electrolyte.

Both the aqueous and solid-state *in situ* XRD apparatuses have been successfully designed, fabricated, and tested in the diffractometer. The use of Be and Kapton windows allow for transmission of the X-ray beam into and out of the apparatus with small amounts of attenuation,

13

on the order of 20%. These apparatuses enable *in situ* XRD during electrochemistry for not just the Pd electrochemical cells presented below but can also be used for testing other electrochemical cells or materials that may only be stable in controlled gaseous or liquid environments.
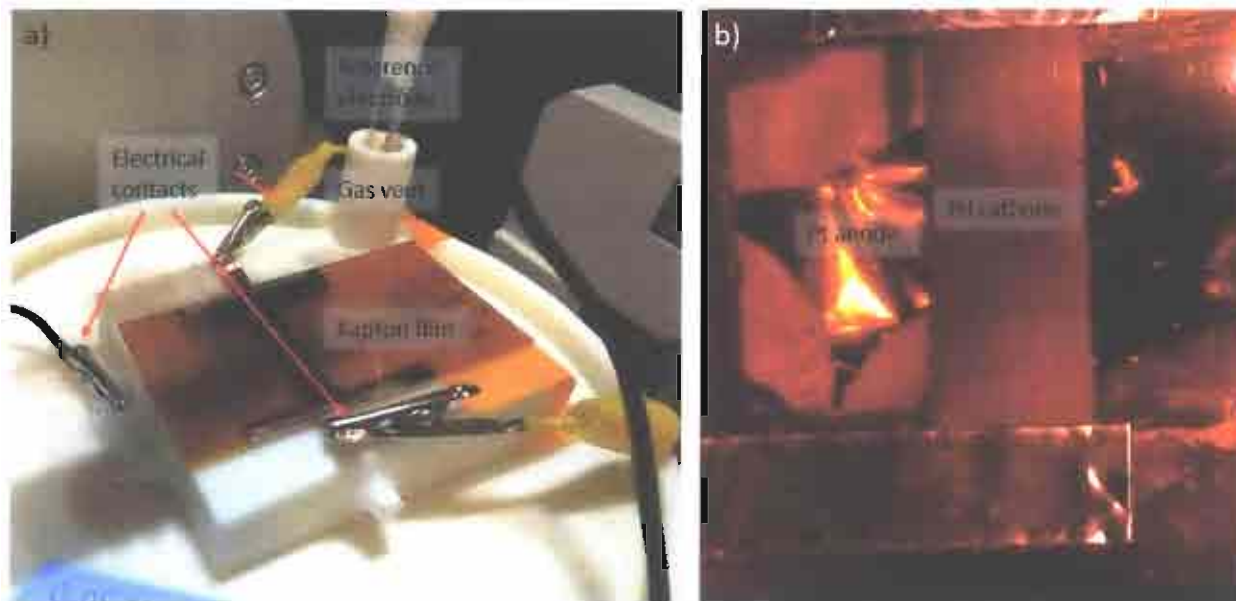

Figure 6. (a) Aqueous *in situ* XRD apparatus consisting of a 3D-printed acrylonitrile butadiene styrene housing with a well for aqueous electrolyte and sealed with X-ray transparent Kapton film on top. A gas vent is located at the corner of the apparatus for excess gas produced during electrochemistry and also houses the Ag/AgCl reference electrode. The top of the apparatus is sloped at a 5° angle to enable bubbles to flow towards the vent. (b) A top view through the Kapton film reveals a Pd cathode that is either sputtered onto the Kapton film as a thin film or attached with Kapton tape in foil form. A Pt foil anode is positioned at the bottom of the well. Electrical contacts are made to all electrodes via alligator clips.

C. Calibration of H:Pd composition to PdH_x lattice parameter

With apparatuses in hand, the next step is to validate the relationship between H:Pd composition and lattice parameter for PdH_x. This study is mainly focused on the higher loaded β-PdH_x phase to the right of the miscibility gap seen in Figure 1. Manchester et al. has shown that the relationship between composition and lattice parameter is linear between $0.7 < H:Pd < 0.9$ [21].

However, the data they used to approximate this relationship at room temperature was actually taken at -196 °C, so the relationship overestimates the loading relative to the lattice parameter due to thermal contraction effects.

A new correlation was created to correct for the above oversight and to improve upon accuracy and better define the uncertainty. Data for β-PdH$_x$ was compiled from several references that included both a XRD lattice parameter measurement and a separate method to measure H content [17-19, 34, 35]. Because these studies were performed at temperatures ranging anywhere from -196 to 800 °C and at pressures up to 10,000 atm, the data were then corrected for temperature and pressure back to standard temperature and pressure using literature values for thermal expansion coefficient and bulk modulus [36-38]. The results are shown in Figure 7. A comparison to the Manchester et al. fit is made as well, showing their over-prediction of the composition for a given lattice parameter. This error can be as high as a 20% overestimation for H:Pd ratio >0.9.
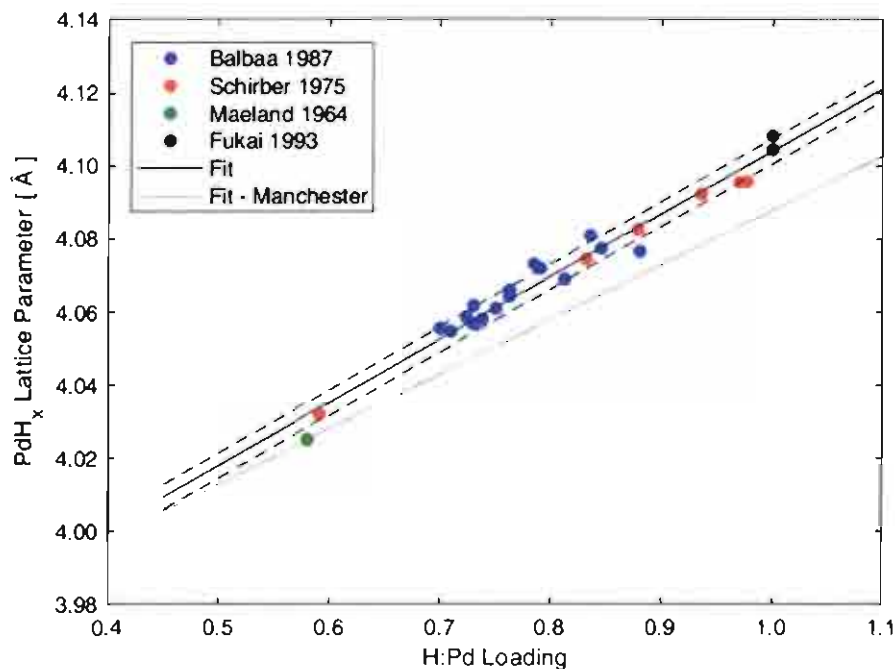

Figure 7. Compilation of lattice parameter vs. H:Pd loading or composition data for β-PdH$_x$ [17-19, 34, 35]. The lattice parameters are corrected for temperature and pressure effects back to room temperature and standard pressure. A linear regression fit of the data is shown as the solid

15

black line with dotted lines on either side representing on standard deviation. The lighter gray line represents a fit derived from Manchester et al. for comparison [21].

A linear regression fit was conducted on the data, and an equation estimating the relationship between lattice parameter and composition was developed:

$$a\,[\,\text{Å}\,] = 3.9321 + 0.1719 \times x,\qquad\qquad\text{(Eq. 1)}$$

where a is the lattice parameter, and x is the H:Pd ratio. Based on the scatter in the data, one standard deviation in the lattice parameter was found to be 0.0034 Å or, when converted to H:Pd ratio, 0.020 deviation in loading. These values represent the error from the fit used in this study. As a comparison, the lattice parameter measurement error itself is only 0.00061 Å, which was found by taking 39 scans of a Pd film, fitting the lattice parameter for each using Rietveld refinement, and calculating the standard deviation.

III.   Electrochemical H insertion in Pd thin films
A. Setup and Protocol

Various electrochemical cells consisting of a cathode, anode, reference electrode, and electrolyte to separate the three are used here. Specific materials and cell structure are described in more detail in the following sections. Pd is used as the cathode, and Pt is typically the anode. A reference electrode is used to monitor the potential of the cathode and anode independently of one another during electrochemistry, allowing for a more accurate representation of cathode potential at various H:Pd composition, which prior studies have not done.

During operation, a potentiostat is electrically connected to the cell, and negative current and potential are applied to induce (1) H_2 gas or liquid H_2O oxidation at the anode to form available H^+, (2) H^+ flowing through the electrolyte, (3) and ultimately H insertion into Pd. A diagram of this process is shown in Figure 8 in the case of H_2 gas. As mentioned previously, in parallel with H insertion is a competing HER process that converts the H^+ directly back to H_2 gas.
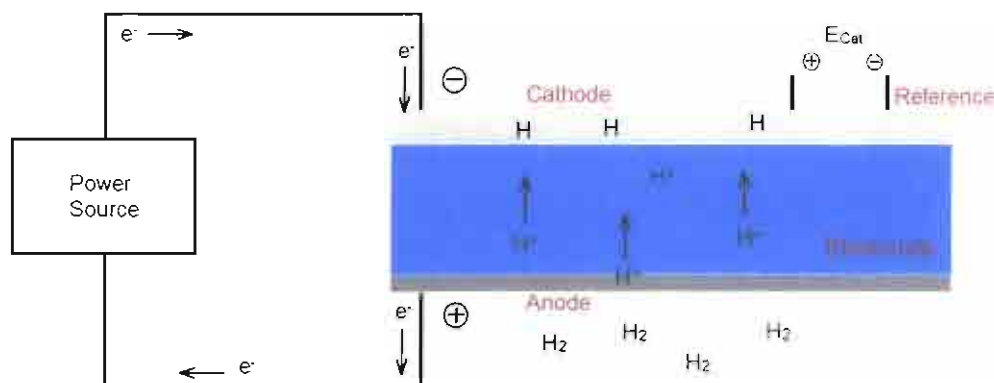
16

Figure 8. Diagram of a 3-electrode cell showing direction of applied potential and current flow during electrochemical H insertion into a Pd cathode. The potential E_{Cat} is the cathode potential against some reference potential.

Current is typically the controlled input in these experiments (i.e., galvanostatic or galvnodyanmic). Because the bulk of the current goes to HER and not the H insertion process, the kinetics are known to follow an exponential Tafel relationship between current and potential. Small changes in potential can produce large changes in current. Therefore, using current as the input and measuring potential permits more careful control of the electrochemical driving force within the confines of our instrument capabilities. Both galvanostatic and galvanodynamic inputs, including both current ramps and steps, are employed to give a wide variety of inputs into the system.

XRD of the Pd cathode is taken during electrochemistry. The diffractometer is set to parallel beam mode, which is less sensitive to height displacement error. Peak shifts of the (111) peak of Pd or PdH$_x$ are monitored, which remain within the 2θ range of 37-41°. An example plot of the raw XRD spectra during an experiment is shown in Figure 9. Here, the peak originally sits at around 40.1°, which corresponds to unloaded α-Pd. As current is applied, the peak begins to shift to the left. Eventually a discontinuity is observed, which represents the miscibility gap between α and β phases. The peak continues to shift to the left thereafter until a maximum loading is reached. In this case a composition of β-PdH$_{0.8}$ was observed. Afterwards, when current is removed from the cell, the peak shifts back to the right due to H naturally desorbing from Pd. Eventually the cathode returns to the α-Pd phase.
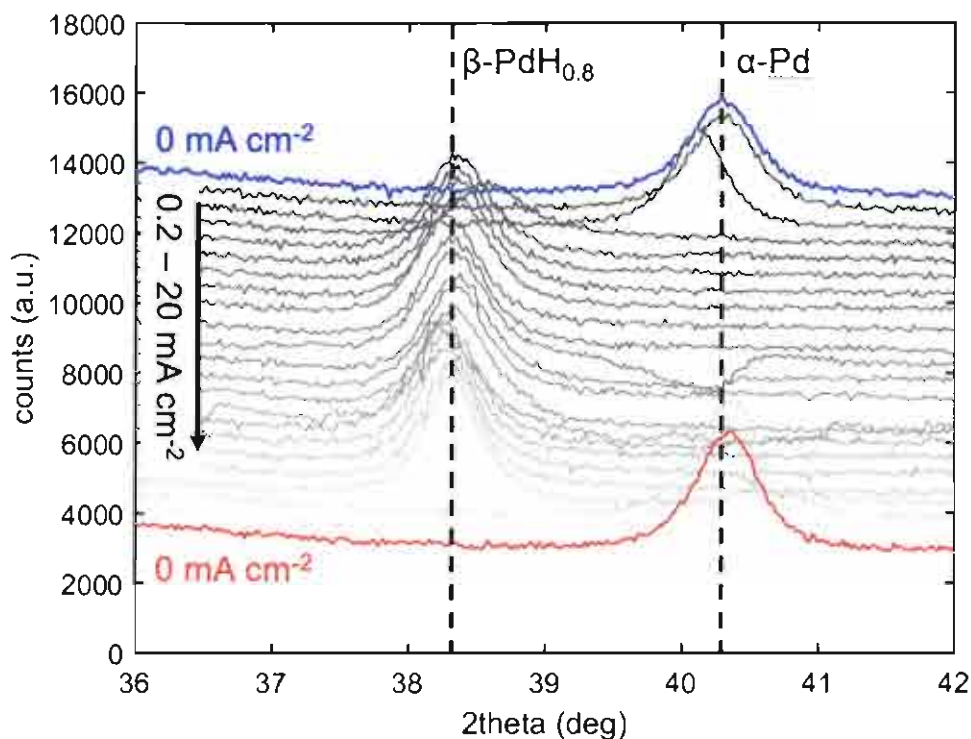
Figure 9. Example raw XRD spectra of Pd cathode undergoing electrochemical H insertion. This set of data is centered around the (111) peak of Pd. The unloaded α-Pd phase peak is located at a 2θ of about 40.1°. As current is applied, the peak shifts to the left. At about 38.2°, a H:Pd ratio of 0.8 is observed. Finally, when current is removed, the peak shifts back to its original position.

The data from these spectra can be converted first to a lattice parameter through either Pawley or Rietveld fitting of the peak position using HighScore Plus (Panalytical). Then using MATLAB (Mathworks) scripts that utilize Eq. 1 for the β phase, the H:Pd ratio is derived from the lattice parameter. In cases when more precise α-Pd phase compositions are needed or for temperatures outside of the two phase regime, both of which are in a regime in which Eq. 1 is not applicable, an equation by Eastman et al. can be used to estimate the composition [39]. Otherwise, the α-Pd phase composition is considered to be at or near 0, consistent with the phase diagram from Figure 1.

18

B. Aqueous electrochemical cells

Traditionally, electrochemical cells used to insert H into Pd have mostly been aqueous. An acidic electrolyte is used to enable H^+ flow from a wire or foil anode to a wire or foil Pd cathode. When H:Pd ratio quantification methods such as resistance ratio are used, a wire format allows for more facile measurements. However, with XRD the difficulty arises from being able to penetrate through the cell, including through the liquid electrolyte, to reach the Pd cathode. Often times a cell is constructed such that in a typical lab-scale X-ray diffractometer, full attenuation of the X-ray beam would occur prior to reaching the detector. That is one of the reasons why synchrotron facilities are more commonly used.

The electrochemical cells in this study are built directly into the measurement apparatus, as shown in Figure 6. The Pd cathode is positioned directly under the 127 μm X-ray transparent Kapton film window. As a 25 μm foil (Beantown Chemical), Pd is mounted using Kapton tape. When a 50 nm thin film, Pd is directly deposited onto the Kapton film using a sputterer (Quorum Technologies Q300TD) at a rate of 10 nm/min. A surface area between 0.8 -1.2 cm^2 is targeted for the Pd in both foil and thin film scenarios. A 25 μm Pt foil (Beantown Chemical) is used as an anode, and a Ag/AgCl electrode in saturated KCl ((Radiometer Analytical) serves as a reference electrode. The entire setup is filled with 0.05 M H_2SO_4 electrolyte. A side view of the setup can be seen in Figure 10.

Figure 10. Side view of aqueous electrochemical cell. A 25 μm Pd foil or 50 nm Pd thin film is attached to a 127 μm X-ray transparent Kapton film. A 25 μm Pd foil is used as anode. An Ag/AgCl reference electrode is inserted into the cell to provide a potential reference. The entire cell is filled with 0.05 M H_2SO_4 electrolyte. An image of the actual cell can be found in Figure 6.

Both Pd foil and thin film cathodes were used to provide a comparison in performance. In both cases current was stepped up sequentially and both the cathode potential and lattice parameter were measured. The results are shown in Figure 11 for two representative Pd foil and thin film cathodes. Current density, cathode potential vs. the reversible hydrogen electrode (RHE) potential, lattice parameter, and composition can be compared between these two different Pd cathode structures. Both current density and potential were averaged over the course of an entire XRD scan. The error in the lattice parameter measurement was deemed minor and was therefore omitted for the purposes of calculating the H:Pd ratio error. Instead an error of ±0.02 one standard deviation of the fit shown in Figure 7.

The thin film loaded to a higher H:Pd composition compared to the foil. In addition, the onset of loading was much faster in the thin film cathode, loading to a H:Pd ratio of over 0.85 almost immediately when -2 mA cm^{-2} was applied. In other thin film samples (not shown here), appreciable H insertion that caused the cathode to transition to the β-PdH$_x$ occurred at current densities as low as -0.1 mA cm^{-2}. Maximum loading observed was close to 0.9. The Pd foil on the other hand loaded to a maximum H:Pd ratio of about 0.78 at -30 mA cm^{-2} and took much longer times to reach near steady state loading values. This observation was consistent among all Pd foils tested in this manner, though in some foils the maximum achieved loading was slightly higher (0.8-0.85).

Thickness is the most intuitive explanation for why the thin film reached higher H:Pd ratios than the foil. If the same flux into both cathodes is assumed, then the thin film has about 500x fewer Pd atoms per H atom entering the cathode. This difference alone could explain the higher H:Pd ratios if faster desorption rates for higher compositions are also considered.

Another possible explanation for the long transient loading times and lower loading values in the Pd foils could be diffusion of H atoms in Pd. Due to the thickness of the Pd foil, diffusion times are significantly longer when compared to the thin film. A rough calculation was performed to estimate the magnitude of this effect. If a H in β-PdH$_x$ diffusion coefficient of 1.26×10^{-11} m^2 s^{-1} is used [40] and assuming 10% of a 30 mA cm^{-2} current density is going to H insertion (which is conservative estimate given that less than that amount is expected), the drop in H:Pd ratio is estimated to be approximately 0.006 across the entire foil cathode. Therefore, it is unlikely that

diffusion is playing a major role. Instead the lower loading values can be better explained by the above thickness hypothesis or other factors stated below. Long transient times for reaching steady state observed in the Pd foil are likely due to just the amount of time needed to pump enough H into the Pd foil at low current densities.
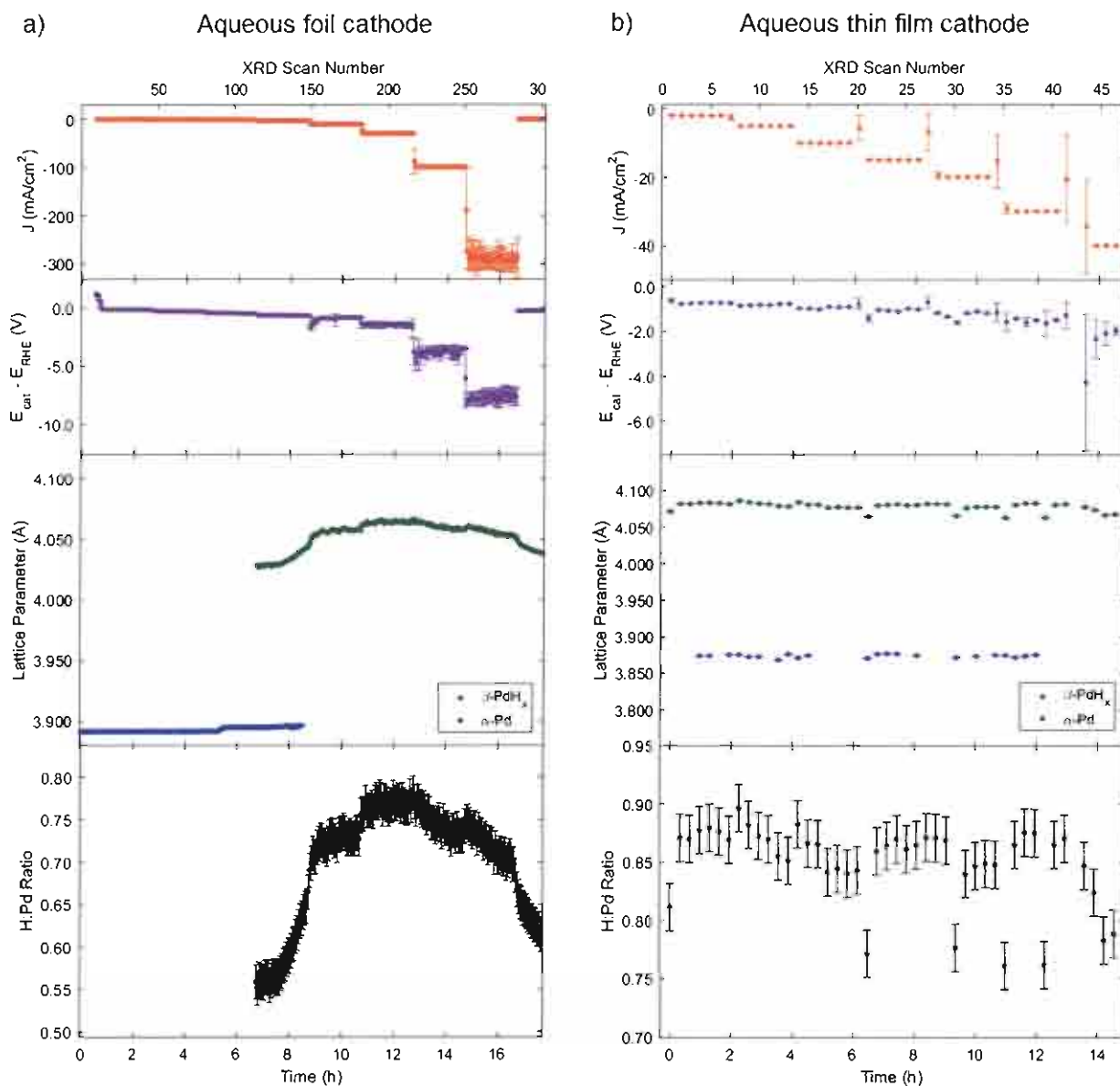

Figure 11. Stacked plots of current density (J), cathode potential vs. the reversible hydrogen electrode (RHE) potential ($E_{cat} - E_{RHE}$), measured lattice parameter, and calculated H:Pd ratio for (a) a Pd foil cathode and (b) a Pd thin film cathode in aqueous cells. Both current density and

potential are averaged over the length of the XRD scan. Error in the H:Pd ratio measurement is ±0.02, derived from one standard deviation of the fit shown in Figure 7.

Several factors other than thickness could play a role in the explaining why thin films reach higher H contents. The Pd thin films deposited on the Kapton film are highly oriented. XRD spectra (not shown here) reveal a (111) plane preference, while Pd foils are found to be randomly oriented. There may be preferential H insertion through these highly oriented films, which could lead to higher observed composition. In addition, slight strain effects from the substrate may cause loading to become more facile for thin films. Finally, different Pd grain size between the thin films and foils may also contribute to differences in H loading. These factors are not examined in detail here and would require further study to elucidate their individual effects.

C. Solid-state electrochemical cells

As stated earlier, using a solid electrolyte rather than an aqueous can provide certain benefits. Higher potentials could be accessed because the stability window of the solid electrolyte is larger than that of water. Higher temperatures can be attained. Lastly, bubble formation should be less of an issue compared to in aqueous media. However, there may be certain disadvantages with using solid electrolytes, such as overall stability of the solid-solid electrode-electrolyte interface and proton conductivity through the solid electrolyte. In order assess the merits of using solid electrolytes, two types of solid-state cells have been constructed with different solid electrolyte materials. The first is a PEM cell using Nafion 117 (Sigma-Aldrich), and the second is a solid oxide cell utilizing $BaZr_{0.8}Ce_{0.1}Y_{0.1}O_3$ (BZCY, CoorsTek Membrane Sciences AS) disks. Both were assessed for their performance in loading H into Pd cathodes.

Nafion electrochemical cells (Figure 12) consist of sputtered a 1.13 cm^2 x 50 nm Pd cathode and 1.13 cm^2 x 10-15 nm Pt anode on either side of a 127 μm Nafion 117 disk. A 10-15 nm thick partial ring Pt reference electrode surrounds the anode. Electrode designs are created using Kapton tape masks. Nafion disks are pretreated in 90 °C 0.5 M H_2SO_4 for at least 1 h and rinsed with 18 MΩ Millipore water and then dried in an oven overnight at 120 °C prior to sputtering.

Similarly, BZCY electrochemical cells (Figure 13) are fabricated using the same electrode sizes as the Nafion cell, except for the deposition of 200 nm of cathode instead of 50 nm, the use of 3-4 nm thick Cr adhesion layers deposited between the electrolyte and all electrodes, and an extra ring of Pd around the cathode in case a Pd reference electrode is needed. The thicker cathode is needed for film stability at higher temperatures, since 50 nm cathodes tend to show signs of dewetting around 400 °C, the operating temperature of the BZCY cell for these experiments. The Pd reference electrode was not used in this study but could be used in the cases when the cathode and anode are exposed to different gas atmospheres.
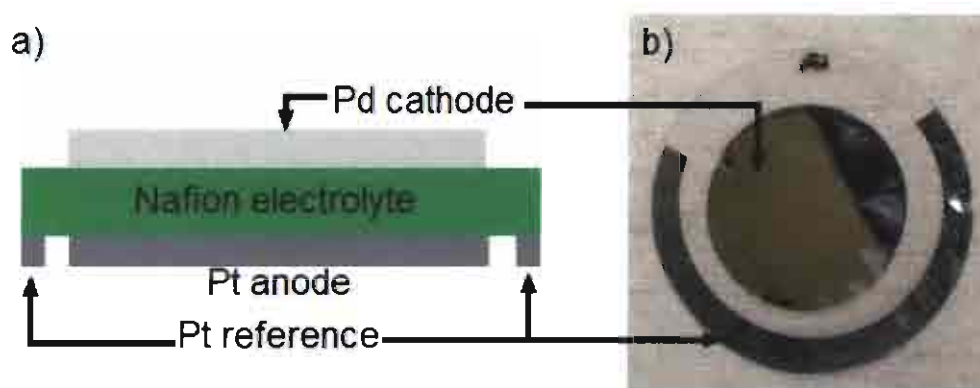

Figure 12. (a) Side view diagram and (b) top view image of Nafion electrochemical cell with 1.13 cm^2 x 50 nm Pd cathode on top, 3.14 cm^2 x 127 μm Nafion 117 electrolyte disk, 1.13 cm^2 x 10-15 nm Pt anode below (not shown in (b)), and partial ring 10-15 nm ring reference electrode surrounding the anode.
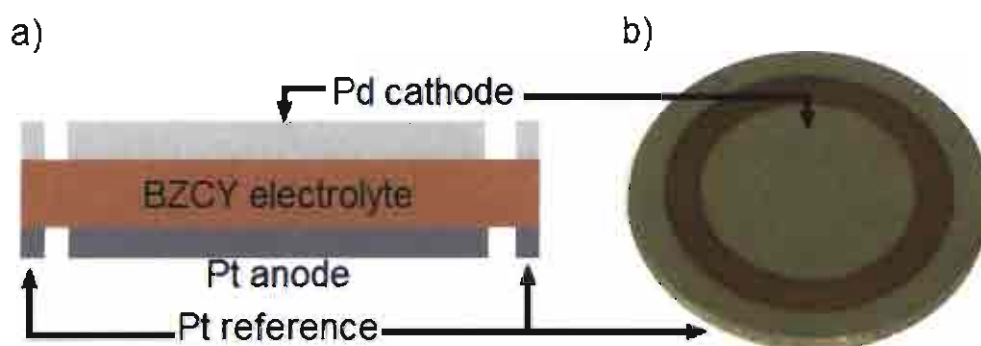
Figure 13. (a) Side view diagram and (b) top view image of $BaZr_{0.8}Ce_{0.1}Y_{0.1}O_3$ (BZCY) electrochemical cell with 1.13 cm^2 x 200 nm Pd cathode on top, 3.14 cm^2 x 1-2 mm BZCY electrolyte disk, 1.13 cm^2 x 10-15 nm Pt anode below (not shown in (b)), and partial ring 10-15 nm ring reference electrode surrounding the anode. The extra ring around the Pd cathode is deposited in case a Pd reference is needed. 3-4 nm of Cr is also deposited between the electrolyte and electrodes to promote adhesion.

The solid-state *in situ* XRD apparatus was used to operate the Nafion and BZCY electrochemical cells. 1 atm humidified H$_2$ gas was flowed in both cases. The Nafion cells were tested at room temperature, while the BZCY cells were brought up to 400 °C. Both current steps and ramps were applied to study the capabilities of these cells to load H into Pd. The results for two representative cells are shown in Figure 14.

The Nafion cell was observed to load up to a maximum H:Pd ratio of about 0.8. This maximum loading was about the same for all Nafion cells than, which was lower than in the aqueous thin films. It should be noted that because the Nafion cells were kept in humidified H$_2$ gas, the starting composition of the PdH$_x$ was higher than that of the aqueous cells, which started at a H:Pd ratio close to 0.

Comparing the Nafion to aqueous thin film cells, the only major difference appears to be the electrode-electrolyte interface. Both types of cells use 50 nm of Pd. Both are on soft polymer substrates. The Pd has (111) preferred orientation in both cases and has a similar grain size. It is hypothesized that a solid-solid electrode-electrolyte interface has poorer stability than a solid-liquid electrode-electrolyte interface, which causes the loading of the Pd cathode in the Nafion cell to be lower. As discussed later, electrochemomechanical damage caused by gas pressure build-up and/or rapid bubble formation interrupts the interface between electrode and electrolyte. In the Nafion case, once the interface is disrupted, robust contact between Nafion and Pd is lost. In the aqueous cell, the interface can self-repair due to the ability of the aqueous electrolyte to flow back around cathode and restore an intimate interface. The loss of contact between electrode and electrolyte appears to be a major cause of not only inability to achieve higher loadings but also a loss of loading at higher current densities.
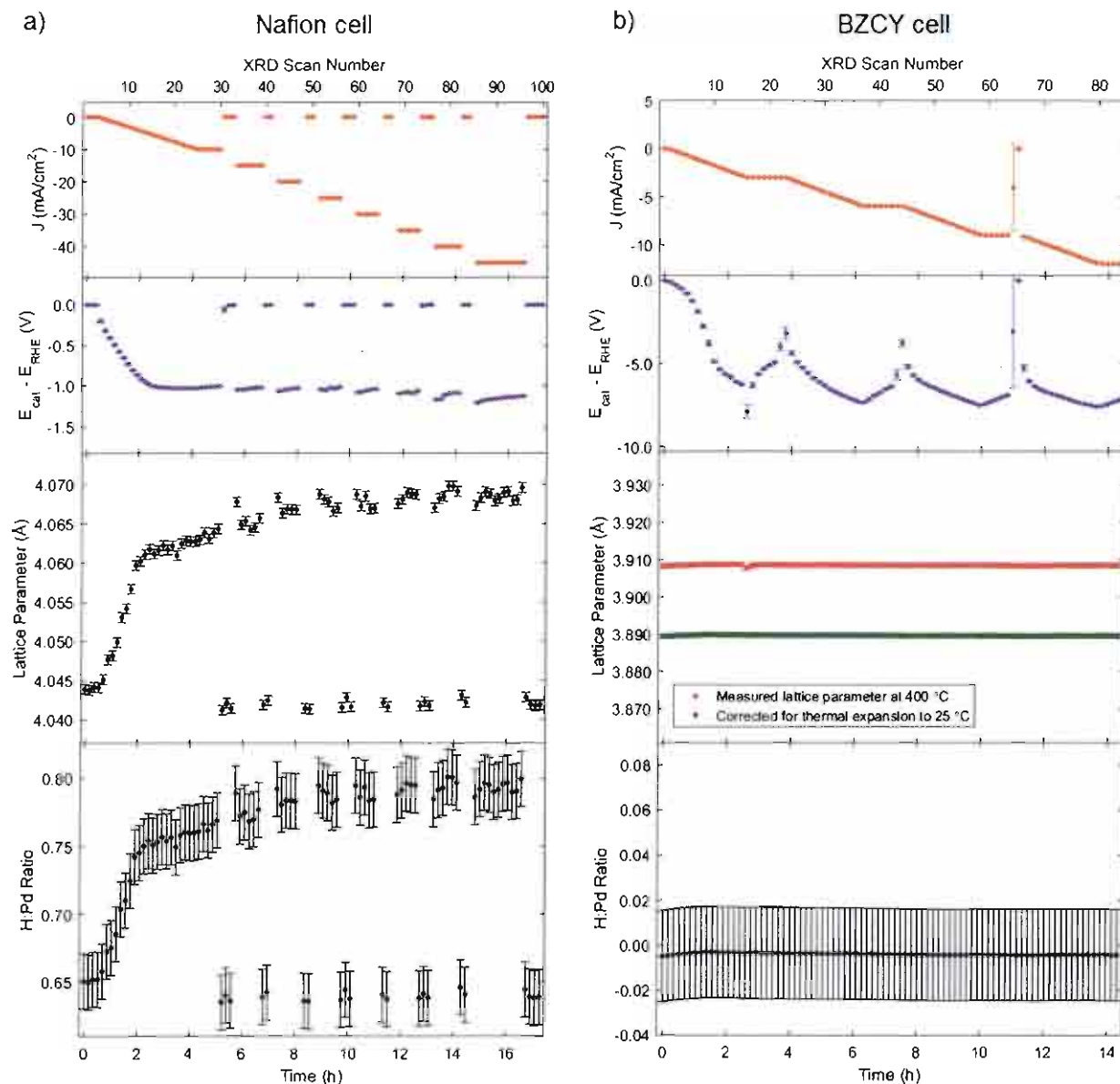
Figure 14. Stacked plots of current density (J), cathode potential vs. the reversible hydrogen electrode (RHE) potential ($E_{cat} - E_{RHE}$), measured lattice parameter, and calculated H:Pd ratio for (a) a Nafion electrochemical cell and (b) a BZCY electrochemical cell. The Nafion and BZCY cells were operated at room temperature and 400 °C, respectively. Both cells were under 1 atm of humidified H_2 gas. Current density and potential are averaged over the length of the XRD scan. Error in the H:Pd ratio measurement is ±0.02, derived from one standard deviation of the fit shown in Figure 7.

The BZCY cell, on the other hand, demonstrated no loading for any of the sample tested. The lack of change in composition is most likely due to temperature effects. At higher temperature there is a larger driving force for H to stay in the gas phase. In addition, the rates of HER are dramatically increased. These two effects combined decrease the likelihood that H will remain in Pd or even insert into Pd in the first place. Though this explanation seems the most plausible, other factors that may contribute to lack of loading include higher resistance of the BZCY ($\sim$1 kΩ vs. $\sim$10 Ω for Nafion) and interface effects between the rigid BZCY and Pd cathode. The former factor may cause most of the potential to be dropped across the electrolyte, leaving less driving force at the cathode interface for H insertion. The interface effects introduce ambiguity because the rigid BZCY, when compared to the compliant Nafion, may restrict the Pd cathode from expanding during H insertion and thus prevent H from entering.

D. Cathode potential vs. composition for different electrochemical cells

A summary of cathode potential vs. composition can be used to make a more direct comparison between the different types of electrochemical cells (Figure 15). The cells with the best performance represented each of their categories, and the potential was increased until either device failure or until the instrumentation limits. The BZCY cells were omitted due to their not having any appreciable loading. The aqueous foil cell did perform beyond the range shown in the plot. However, the H:Pd ratio of the cathode plateaued and began to decrease, so the range was kept smaller to show more detail at potentials closer to 0.

From the plot in Figure 15, it can be clearly seen that the aqueous thin film had the highest achieved H:Pd ratio of 0.96. The aqueous foil followed thereafter at 0.83. The Pd cathode in the Nafion cell loaded even less with a H:Pd ratio of 0.81. From this ranking, it can be gathered that the largest effect on loading is temperature, so lower temperatures should be used to maintain higher loading. Next, aqueous electrolytes appear to create the more robust interface needed for to achieve and maintain higher H content. Lastly, using thin films instead of foils seem to be able to take H:Pd ratios close to 1. There is some variability in the results from sample to sample, but the overall trends between these different electrochemical cells are consistent.
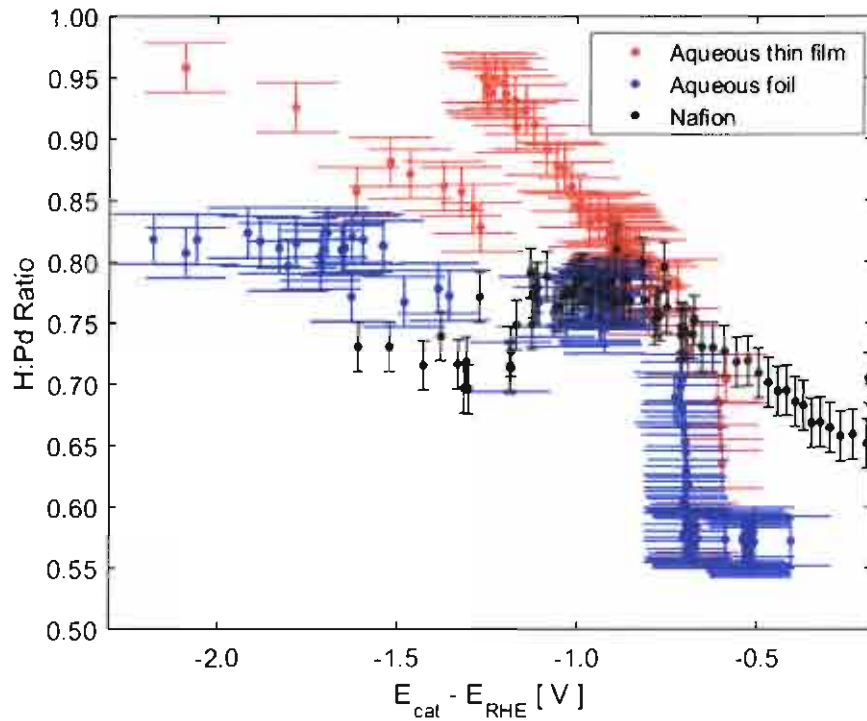
Figure 15. H:Pd composition vs. cathode potential ($E_{cat} - E_{RHE}$) for the aqueous foil, aqueous thin film, and Nafion electrochemical cells with the highest H loading. BZCY cells were omitted because no appreciable loading was observed.

E. Failure modes

One important factor that limits higher compositions is cell failure. For every cell, there is some maximum current density that can be applied before the loading begins to decrease. For thin films, the cause of this phenomenon is most likely electrochemomechanical damage, which is caused by a combination of expansion/contraction effects from H insertion, bubbles in the case of aqueous cells, and gas buildup between at the electrode-electrolyte interface that causes delamination or spalling of the cathode. As this damage occurs, the observed loading begins to drop, most likely due to cracks forming that isolate some areas of the cathode. When there is enough damage, the cell can catastrophically fail, and little to no current can be applied thereafter.

An example of this macroscale electrochemomechanical damage can be seen in an aqueous thin film cell seen in Figure 16. Here, as the current was stepped up, the H:Pd ratio increased to a saturation point, after which a plateau in the loading was created. At some critical current density, the Pd film became damaged enough that the cell catastrophically failed. Afterwards, no current could be applied to the cell.
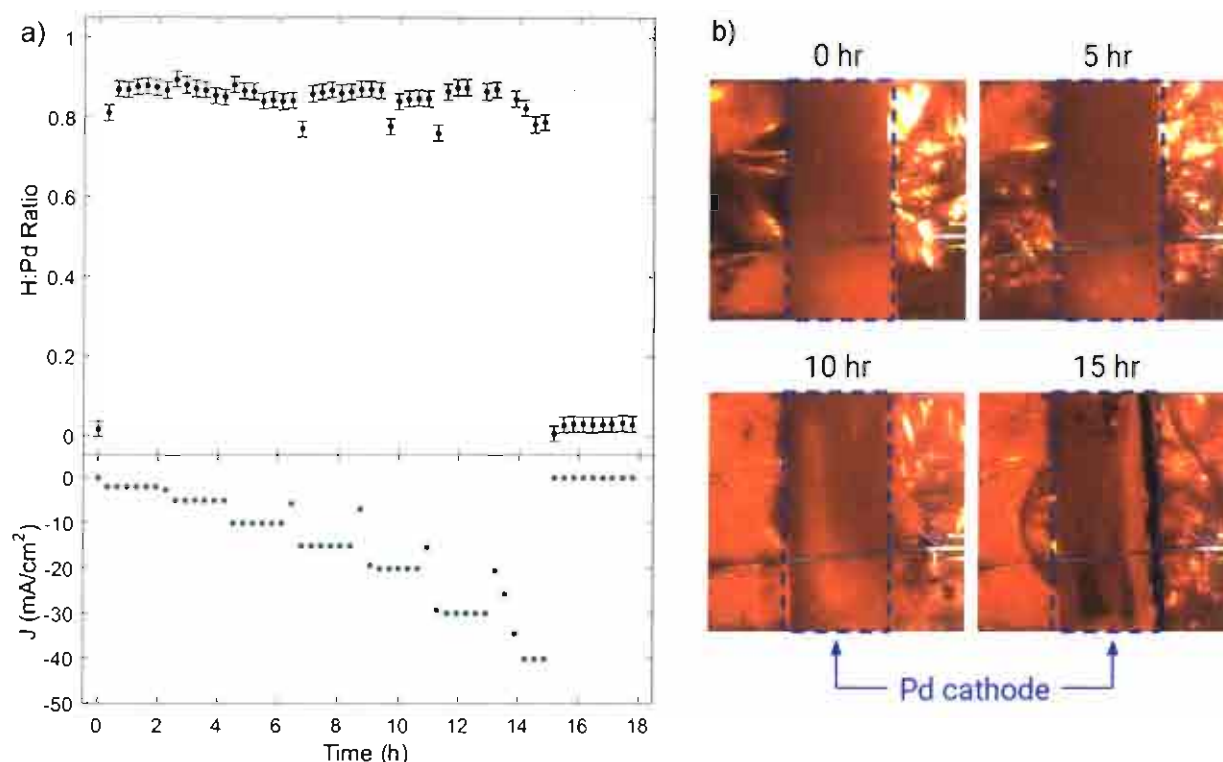

Figure 16. An aqueous thin film cell undergoing H insertion showing (a) increasing applied current density (J) that increases H:Pd ratio at first until catastrophic failure of the cell at 15 h. (b) Corresponding images of the Pd cathode showing electrochemomechanical damage to the film as current is increased.

Figures 17-19 show the electrochemomechanical damage for all thin film Pd electrodes after electrochemistry. These micrographs were taking with a scanning electron microscope (SEM, FEI Helios). Cracking and delamination appear to be the predominant issues. The aqueous thin film cathode shows cracks on the order of 10 μm, which were mostly caused by expansion and contraction of the Pd lattice. The orientation of these cracks could be due to the stress profile of the Kapton film if uniaxially or biaxially stretched during its manufacturing.

The Nafion cell case displays cracks that form domains on the order of 10 μm. These domains may have become entirely isolated during cell operation and decreased the overall loading. The more uniform character of the cracks could be due to the Nafion itself swelling from hydration when exposed to humidified H_2. It is likely a combination of that and the expansion/contraction of the Pd during H insertion.

In the case of BZCY cell, even entire grains of BZCY on the order of 100 μm were found to have blown off the surface. Despite not having loaded any H into Pd, the BZCY cell clearly shows that H^+ still flowed vigorously across the electrolyte to the electrode-electrolyte interface. Pores at the surface of the BZCY disk may have provided a location for H_2 gas to evolve. The resulting trapped gas could have built enough pressure to cause the film to rupture, and in some circumstances take entire grains of BZCY with it.
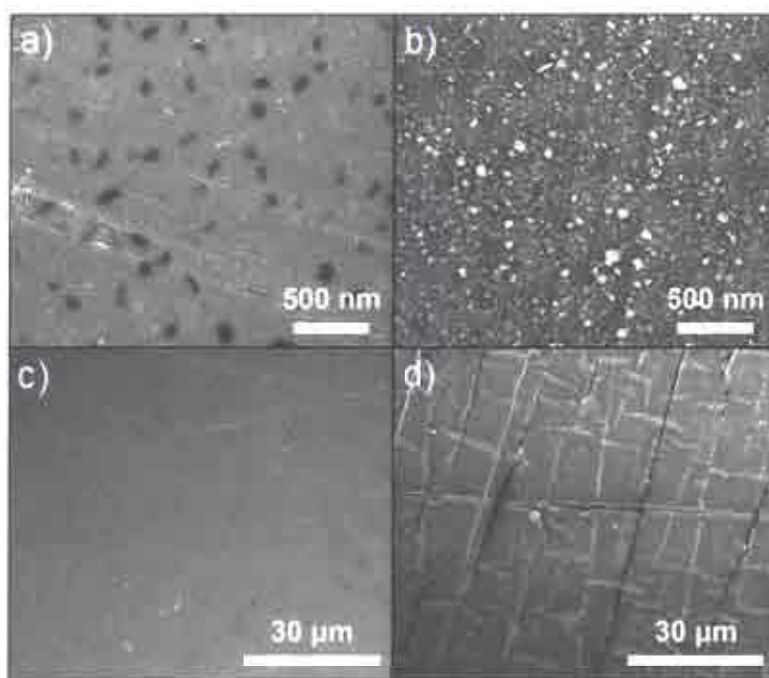

Figure 17. Scanning electron micrographs of an aqueous thin film cell Pd cathode before (a, c) and after (b, d) electrochemical H insertion. 10 μm cracks and surface roughening, as well as what appears to be partial delamination, can be observed after H insertion.
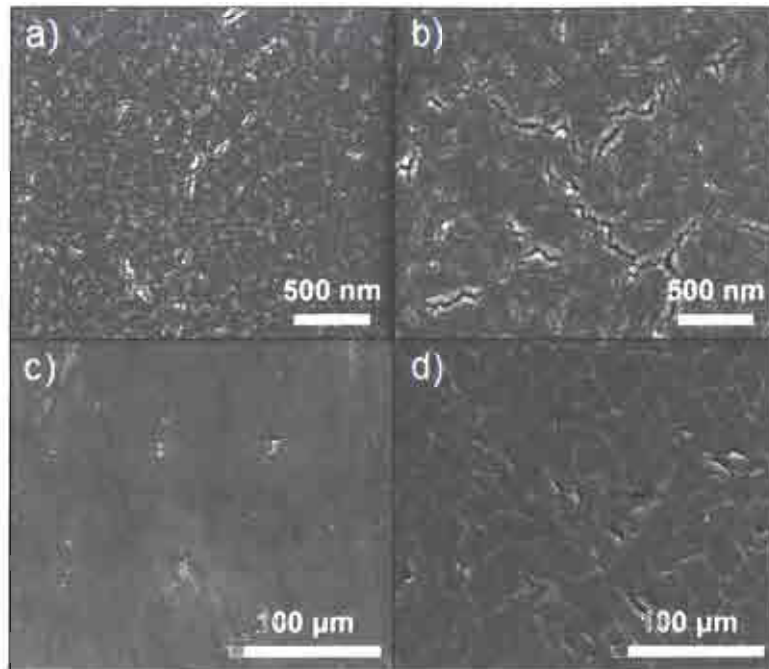
Figure 18. Scanning electron micrographs of a Nafion cell Pd cathode before (a, c) and after (b, d) electrochemical H insertion. 1-10 μm cracks and delamination are observed after H insertion.
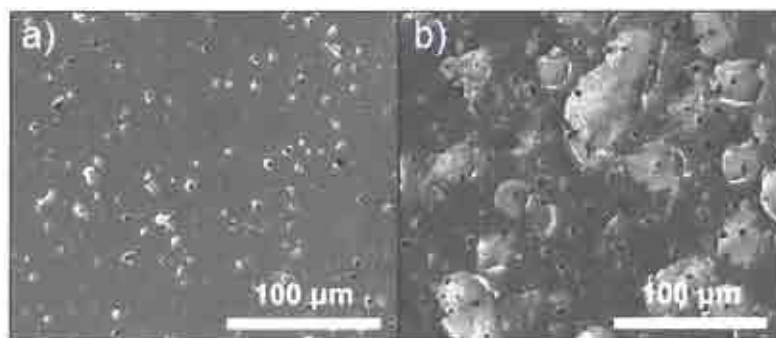

Figure 19. Scanning electron micrographs of a BZCY cell Pd cathode before (a, c) and after (b, d) electrochemical H insertion. Large grains of BZCY have blown off the surface after H insertion. Some film blistering without the Pd film completely the surface can also be observed.

The Pd foil behaved differently than the other thin film cathodes. Scanning electron micrographs show that cracking and delamination were not issues, the latter due to the fact that there was nothing from which the foil could delaminate (Figure 20). Instead deposits appeared to have built

up on the surface of the cathode. The elemental makeup of this surface contaminant was investigated with energy dispersive x-ray spectroscopy during SEM imaging, and it was found to consist of Cu and Pt. Cu tape was used as current collectors in the cell, so trace of amount of Cu could have dissolved into the electrolyte, while Pt contamination originated directly from the Pt anode. These elements were most likely electrodeposited on the surface of the Pd cathode at higher applied potentials.
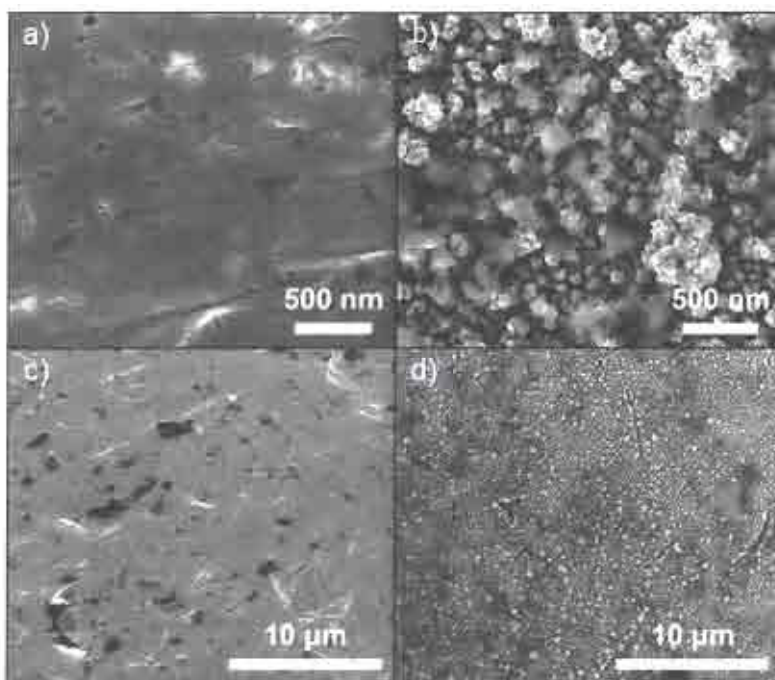

Figure 20. Scanning electron micrographs of an aqueous foil Pd cathode before (a, c) and after (b, d) electrochemical H insertion. Surface roughening and deposits appear on the surface after electrochemistry. These features were found to be Cu and Pt that most likely electrodeposited onto the Pd surface when applied potential was larger.

Although the Pd foil cathodes do not suffer from cracking and delamination, the deposition of these contaminants can hinder the performance of the cell. If enough buildup occurs, H would not be able to enter the Pd foil. Furthermore, having Pt at the surface of Pd cathode probably increases the rate of HER, which reduces the amount of current going to H insertion.

Another issue that the aqueous cells suffer from is bubble formation, a phenomenon that is especially prominent at the high currents needed by Pd foil cathodes. If bubbles form around the surface of the Pd, they can disrupt the electrode-electrolyte interface and prevent H^+ from reaching the cathode. This problem may be another reason why the foil cathodes cannot load to higher H:Pd ratios.

F. Key takeaways for achieving higher H content in Pd

The concepts learned from investigating these different electrochemical cell formats can be distilled into the following four statements:

(1) Thin films load better than thicker foils, likely due to the higher H flux per atom of Pd.
(2) Liquid electrolytes enable higher achievable H:Pd ratio compared to solid electrolytes due to the ability for the solid-liquid electrode-electrolyte interface to self-repair.
(3) Higher temperatures favor HER and gas desorption and therefore inhibit loading.
(4) Limiting electrochemomechanical damage in thin films can increase overall loading.

By applying these concepts to future studies of electrochemical H insertion in Pd, reproducible, high H loadings can hopefully be achieved.

IV. Additional work on solid electrolytes at elevated temperatures

Despite the lack of observed H loading in electrochemical cells at elevated temperatures, high temperature solid oxide electrolytes, such as BZCY, are still an interesting field of study for applications in fuel cells, electrolyzers, and CO_2 reduction [23, 41, 42, 43]. Two areas of investigation are described here: (1) the synthesis of single crystal $BaZr_{0.85}Y_{0.15}O_3$ (BZY) for lower temperature operation and improved mechanical properties and (2) high temperature *in situ* calorimetry of solid electrolyte cells under electrochemical cell operation. The former would potentially allow solid oxide electrolyte operation in the 150-250 °C range that is currently largely inaccessible. The latter can complement electrochemical data in determining the stability and life of various solid oxide electrolytes during operation. This technique is used in ambient

temperature electrochemical cells such as batteries today but has not been implemented for fuel cells or electrolyzers operating at elevated temperatures [44-46].

A. Attempted growth of single crystal BZY

BZCY is considered to be on the lower temperature spectrum for solid oxide fuel cells, being able to operate in the 300-500 °C range [47] and having a proton conductivity of ~0.4 mS cm^{-1} at 500 °C [48]. However, further improvements to BZCY could allow its operation at even lower temperatures without having to resort to thin films, which have potential issues with mechanical stability and electrical shorting from film discontinuities. Density functional theory (DFT) and experimental analyses of BZCY have shown that grain boundary resistance can lower overall conductivity by as much as 3 orders of magnitude [49-54].

Single crystal BZY would be able to significantly improve conductivity by eliminating grain boundary resistance. BZY is targeted for single crystal growth instead of BZCY because the Ce is not needed as a sintering aid. Due to the high melting point of BZY, which is close to that of $BaZrO_3$ (BZO) at around 2,500 °C [55, 56], the method of choice was optical floating zone growth in a 4-mirror Xenon floating zone furnace (Crystal Systems Corporation) at the Johns Hopkin University's Platform for the Accelerated Realization, Analysis, & Discovery of Interface Materials (PARADIM).

BZY powder (CerPoTech) mixed with various amounts of BaO (Sigma-Aldrich) was first pretreated at 1,600 °C in air for 8 h to remove moisture and increase grain size. The powder was then pressed into rods and sintered at 1,600 °C for 8 h. Two rods of the same composition were mounted to the float zone furnace. The chamber was flushed with Ar for 10 min and then the rods were heated to 2,400 ± 100 °C to begin growth. Growth rate was set between 10-20 mm/min, which although on the faster side, was needed to reduce the amount of Ba loss during the melting process.

Two BZY crystal rods of about 3 mm in diameter were grown, one using pure BZY with no BaO and another with 7.5 wt% BaO added (Figure 21). XRD of the two samples revealed that a large amount of $Zr_{1-y}Y_yO_2$ (0 < y < 1) impurity was present, likely due to the rapid evaporation of BaO from the melt. The pure BZY rod contained anywhere between 25-49 wt% impurity depending

on position along the rod. The sample with BaO added contained less impurity (18-45 wt%). Based on these results, it was determined that adding excess BaO reduced the level of impurity present after processing through the floating zone furnace. However, the effects are limited by the stability of the rods. Because BaO is very hygroscopic, adding BaO in excess of 7.5 wt% caused the mixed powder of BZY and BaO to not pack well even after pretreating to dry the powder. The rods that were formed were unable to be sintered without breaking.
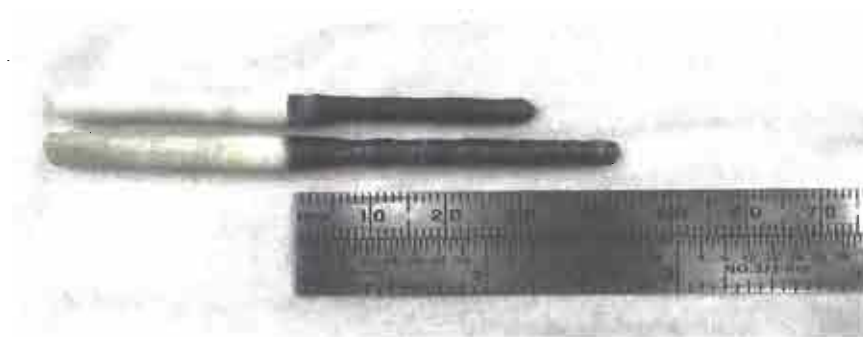

Figure 21. $BaZr_{0.85}Y_{0.15}O_3$ (BZY) crystal rods grown in an optical float zone furnace. Rods were approximately 3 mm in diameter. One rod was grown from pure BZY, while the other was grown with an added 7.5% wt BaO to reduce the effect of BaO evaporation from the melt.

Despite not having pure single crystal samples, these rods were still cut into disks and analyzed further. Area XRD was performed on the BZY sample with added BaO using a D8 general area detector diffraction system (GADDS) multipurpose diffractometer (Bruker), shown in Figure 22. A qualitative assessment of the resulting spectrum shows multiple spots and small bands around each concentric circle, indicating multiple grains present in the sample. Brighter spots mixed in with darker spots suggest a distribution of both large and small grains. SEM shows that the BZY grains in the sample are on the order 10-100 μm but that there are also $Zr_{1-y}Y_yO_2$ impurities in between the grains on the order of 1 μm in size (Figure 23). The darker and lighter areas in the SEM corresponding to BZY and $Zr_{1-y}Y_yO_2$, respectively, were confirmed via elemental analysis by EDX.
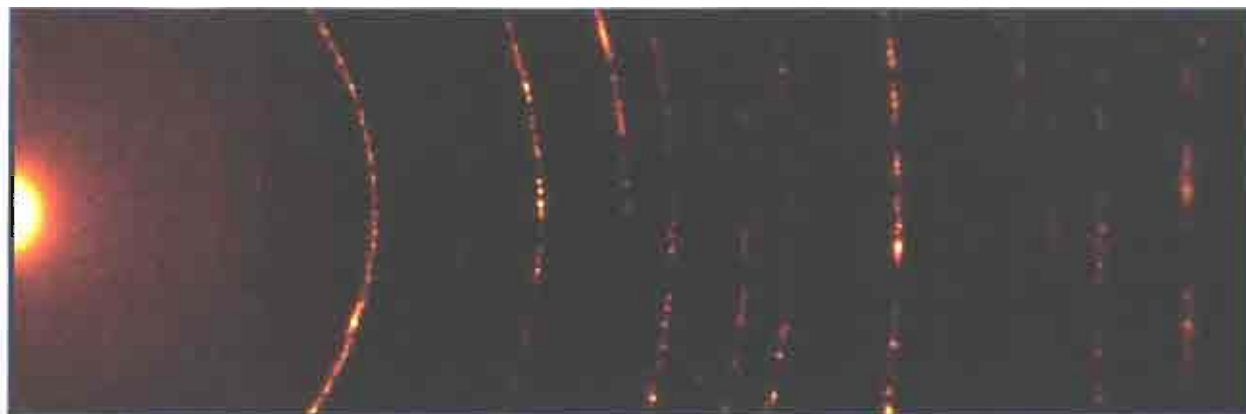
34

Figure 22. Area diffraction spectrum of a BZY grown crystal rod. Large bright spots indicate the presence of large grains. Multiple darker spots and small bands indicate that the crystals are not single crystals.
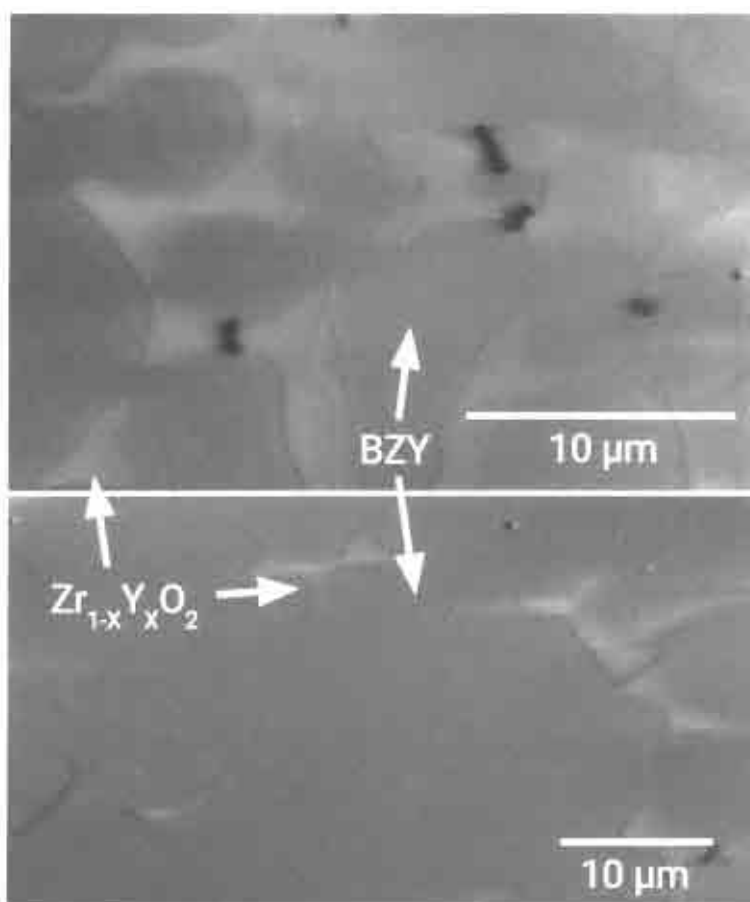

Figure 23. Scanning electron micrograph of BZY crystal rods showing the presence of impurity $Zr_{1-y}Y_yO_2$ phase in a BZY matrix.

The BZY disks were tested to see if the larger grain size and therefore fewer grain boundaries had improved the overall conductivity of the material. 3.14 mm^2 x 20 nm thick Pt electrodes were sputtered onto a BZY disk with about 20 wt% $Zr_{1-y}Y_yO_2$ impurities (Figure 24). The samples were mounted into the solid-state *in situ* XRD apparatus for the purposes of just performing electrochemistry. 1 atm of humidified H_2 was flowed into the apparatus. The BZY sample was heated between 300-600 °C and cyclic voltammetry between -1 and 1 V was performed. The conductivity was extracted from the slope of the potential vs. current profile at each temperature.
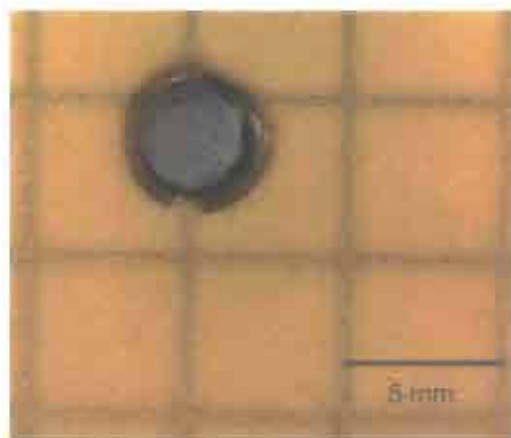
Figure 24. A BZY crystal sample coated with sputtered 3.14 mm^2 x 200 nm thick Pt electrodes.

The BZY conductivity was compared to that of a comparable BZCY disk. The results shown in Figure 25 reveal that there is no significant difference in the conductivity between the BZY and BZCY electrolytes. The conductivity gains from having larger grains in the BZY samples are likely offset by the presence of impurities. Therefore, unless the BaO evaporation issue can be resolved, BZY crystals grown by the optical floating zone method do not provide any obvious advantages compared to BZCY disks.

Figure 25. Comparison of conductivity vs. temperature of grown BZY crystals and commercial BZCY electrolytes. Both electrolytes have 20 nm sputtered Pt electrodes deposited on either side.
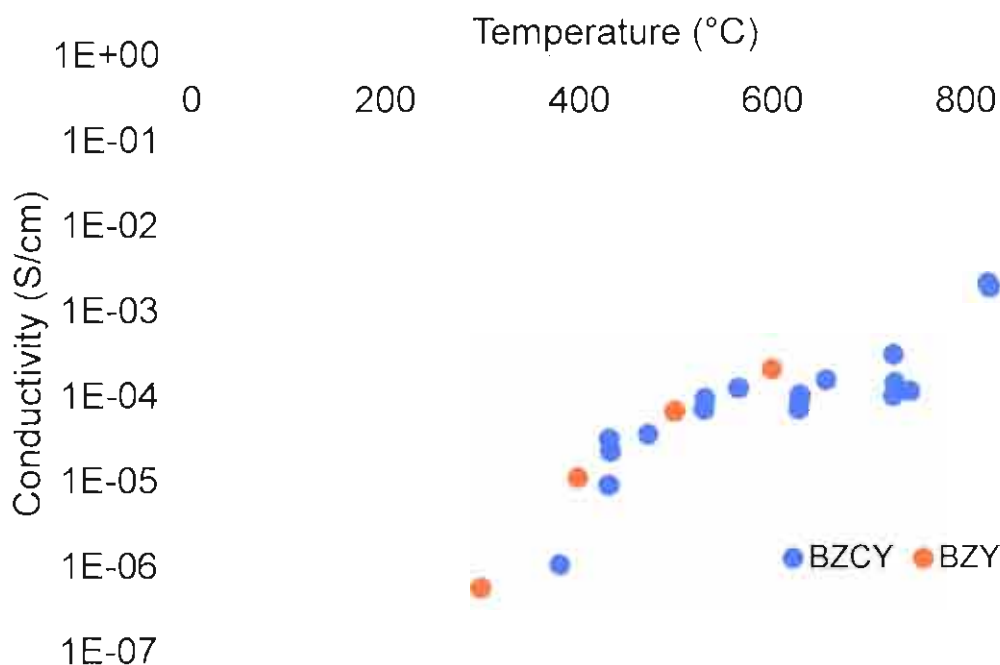
B. High temperature calorimetry of solid oxide electrolytes

In order to investigate the stability of solid oxide electrolytes operating in an electrochemical cell, a high temperature *in situ* calorimeter can be used to detect and quantify degradation products or side reactions. This calorimeter needs to meet all of the working conditions of such a cell. As mentioned above, the applications for this apparatus include studying fuel cells, high temperature electrolysis, and CO_2 reduction to create synthetic fuels. Typically, differential scanning calorimetry is used to determine the temperature stability and degradation rates of these solid oxides [57-60], but this *ex situ* method does not include the operating electrochemical conditions that may contribute to the degradation of these materials.

A ProboStat[TM] (Norwegian Electro Ceramics AS), a commercially available apparatus used to study high temperature electrochemical cells, is modified with temperature probes to fit the operating window of solid oxide electrochemical cells. This *in situ* calorimeter features the ability to perform electrochemistry at different temperatures in the presence of different gas

37

streams exposed to the cathode and anode of an electrochemical cell. It is also able to withstand both oxidizing and reducing gas environments. Combined with electrochemical methods, calorimetry allows for assessment of relevant thermodynamic and kinetic parameters that relate to the long term performance of these electrochemical cells.

i.   Calorimeter design objectives

The design objectives for the calorimeter are laid out in Table III. The temperature range allows for operation of a wide variety of solid oxide electrolytes. The potential and current capabilities are suitable for the electrochemical cell sizes and shapes that were used in the previous sections for H insertion experiments. The number of electrical connections enable a minimum of two sets of temperature probes (each requiring two connections) and connections made to the cathode and anode of the cell, which total to six. Additional connections can be made to enable four-point measurement capabilities, as well as the use of a reference electrode, to sum up to 11 total connections. The ProboStat^{TM} is designed to allow a cell to be sealed such that the anode and cathode sides can be exposed to isolated gas streams, which is needed in fuel cell operation.

Table III. Design objectives for *in situ* calorimeter.

Specification	Design objective
Temperature	20 - 1,000 °C
Potential range	±20 V
Current range	Up to 400 mA
Electrical connections	6 - 11
Gas streams	1 - 2
Sample diameter	10 - 30 mm
Power sensitivity	< 50 mW

The power sensitivity required is taken from expected power density of these solid oxide electrochemical cells. For purposes of simplifying the analysis, only fuel cells were considered, which have an electrical power density in the range of 500-2,000 mW cm^{-2} and an efficiency of about 50% [61, 62]. If considering the low end of this range the total power input is about 1,000 mW cm^{-2} with 500 mW cm^{-2} lost as heat. If 10% of that heat loss is set as the sensitivity bar (i.e.,

being able to detect power changes of more than 10% due to degradation or other effects), then the power sensitivity must be at most 50 mW for the ~1 cm^2 sized cells used in this study. As an additional check, degradation reactions from a typical solid oxide electrolyte under certain thermal conditions is on the order of 100 mW/g [63]. The BZCY disks used here have a mass of at least 1 g, so degradation rates should exceed 100 mW in many cases. Therefore, the power sensitivity limit of 50 mW is sufficient.

ii.   *In situ* calorimeter design

The calorimeter is presented in Figure 26. A ProboStat™ is fitted with thermocouples. An electrochemical cell or sample with dimensions between 0.5-10 mm in thickness and 10-30 mm in height with an attached resistance thermal detector (RTD), described in more detail below, is mounted onto the inner tube. The apparatus is put inside an 18" vertical tube furnace (Mellen). There is an option of sealing the cell with a Au ring to the inner tube to allow simultaneous flow of two separate gas streams, one through the inner tube and the other through the outer tube. The cathode and anode of the electrochemical cell would each be exposed to only one of these gas streams. For the purposes of testing the calorimeter, this option was not used.

The outer tube of the ProboStat™ can either be made of alumina for operation at temperatures >600°C or quartz for temperatures below that. The internal parts, including the inner tube, shields for wires, and support posts are all made of alumina. Wires are either Pt or Ru-Pt alloy. All together, the apparatus withstand temperatures in excess of 1,000 °C.

 The thermocouples in this apparatus take temperature of the furnace wall (T_{fw}), a location proximal to the sample (T_{prox}), and the temperature of the room (T_{room}). The furnace wall and room thermocouples are K type, while the proximal is S type (Omega). These thermocouples are connected externally to an eight-channel data acquisition module (Omega). The RTD on the sample takes a temperature close to that of the sample itself (T_{RTD}). All of these temperature probes are used in conjunction to get an approximation of the heat flowing through the sample and its surroundings.

Electrical connections are wired to the electrochemical cell's cathode and anode, as well as to the proximal thermocouple, and connected through the available ports of the ProboStat™ to a

potentiostat (Bio-Logic). The potentiostat is able to meet the electrical design criteria stated in Table III. Humidified H_2 or Ar gas is plumbed to the ProboStat^{TM} without any significant modification to the apparatus. Gases are flowed in between 5-20 ml/min and removed through an outtake vent.
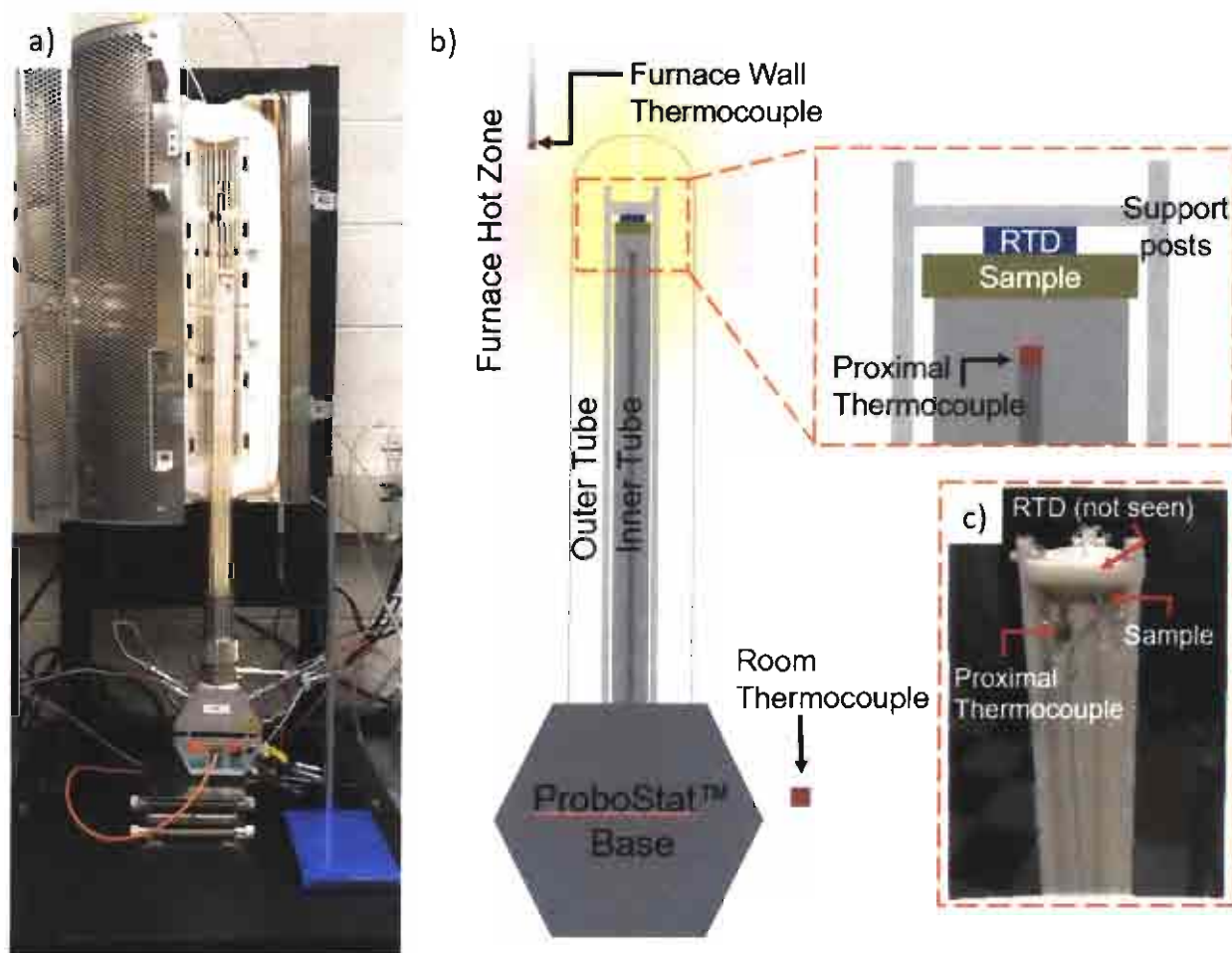

Figure 26. (a) The ProboStat^{TM} calorimeter inside an 18" vertical tube furnace. (b) A diagram of the calorimeter with thermocouple and sample placement, and (c) an image of the setup within the outer tube. Thermocouples are mounted to the furnace wall, the outside of the inner tube, and to a location next to the calorimeter that can be capture the temperature of the room. The sample (electrochemical cell) is mounted into the apparatus and secured down with support posts. The sample can be sealed to the inner tube if two gas streams are used, one flowing through the inside of the inner tube and one flowing in the outer tube. Gas and electrical lines not shown.

iii. Electrochemical cell design

The electrochemical cells used here are nearly identical to the BZCY cells shown in Figure 13. The only differences are (1) a 20-200 nm Pd or Pt cathode that spans the entire surface of the BZCY disk instead of just part of it and (2) a Pt thin film RTD (US Sensor or Omega) that is cemented on top of the cathode. A diagram and image of the electrochemical cell with attached RTD is shown in Figure
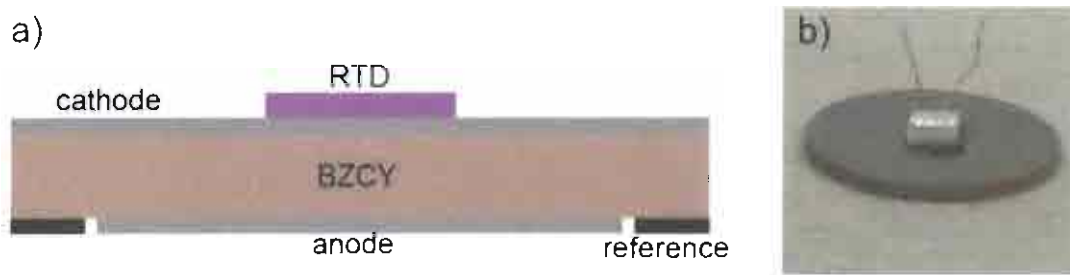

Figure 27. (a) Schematic of BZCY electrochemical cell fabricated similar to in Figure 13. A resistance temperature detector is cemented to the top of the cathode. (b) An image of the cell with RTD.

iv. Modelling the *in situ* calorimeter

The *in situ* calorimeter can be modelled using an equivalent circuit model that traces all of the heat flows from the various heat sources present. The goal is to look for the simplest model that can capture enough of the system dynamics to meet the heat sensitivity requirements laid out in the design objectives. The model selected uses a grey-box approach that combines input data with some fitted system parameters that are roughly based on the physics of the apparatus. The inputs of such a model are the temperatures measured and the input powers into the system. The output is the actual power detected by the calorimeter. At first, a calibration is performed during which both inputs and outputs are known or can be estimated. A system identification process takes those inputs and expected outputs and fits the parameters of the model such that inputs

going into the model create those expected outputs. Once calibrated, this model can then be used to predict the expected power output given a new set of inputs into the system.

The equivalent circuit model upon which this model is based is presented in Figure 28. Several iterations were made on model prior to finding one that represents the physics of the system well without introducing too many parameters (i.e., overfitting). A physical diagram of what the nodes in the model represent is also shown in Figure 28. This model expects power to flow from the furnace (T_{fw}) down through the RTD (T_a) and then through the sample (T_b), and then out through the inner tube measured by the proximal thermocouple (T_{prox}) and the room temperature thermal ground (T_{room}). Powers can be generated at (1) the RTD when a sense current is applied to measure its resistance, (2) the sample when current is applied between the anode and cathode (P_{ion}) or across the cathode (P_{cat}). P_{cat} is used to mimic surface degradation of the electrolyte, assuming that degradation occurs at the interface between the cathode and electrolyte.
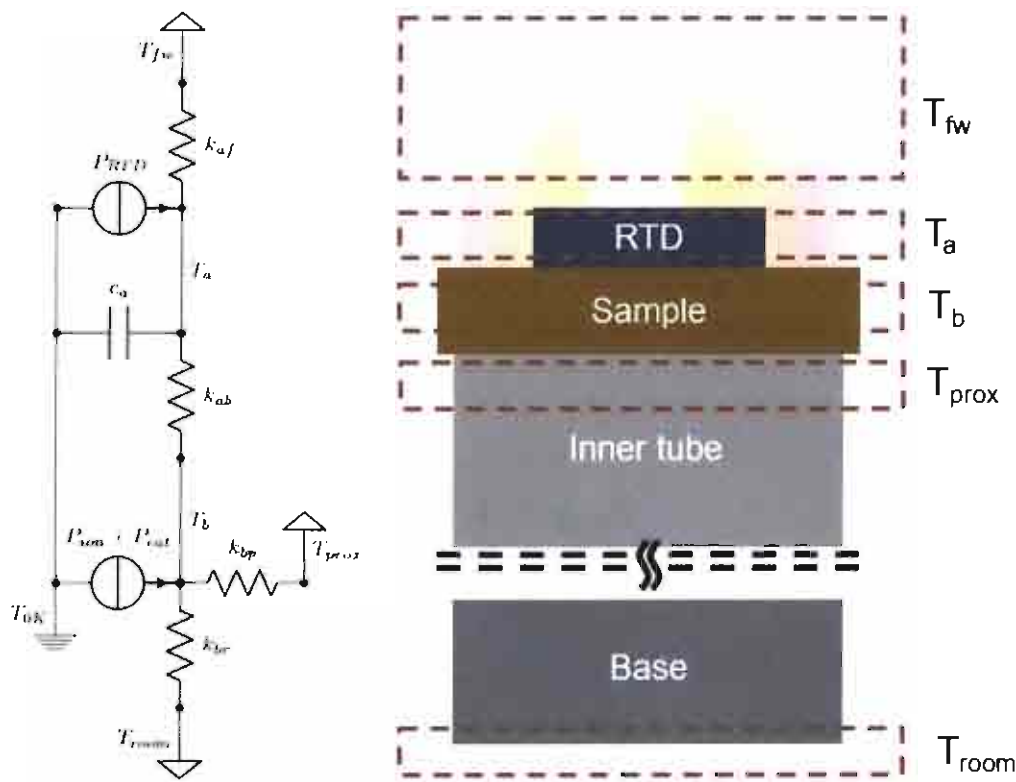

Figure 28. (a) Equivalent circuit model of the *in situ* calorimeter and (b) a physical diagram of what each node in the circuit model represents in the calorimeter. Heat flow is expected to stem

from the furnace (T_{fw}) and flow through the RTD (T_a), the sample itself (T_b), and out through the inner tube (T_{prox}) to a room temperature ground (T_{room}). Power can be generated at the RTD (P_{RTD}) and at the sample (P_{ion} and P_{cat}) through the application of current.

The following system of equations can be used to describe the equivalent circuit:

$$\frac{dT_a}{dt} = \frac{1}{c_a}(P_{RTD} + k_{af}(T_{fw} - T_a) - k_{ab}(T_a - T_b)),$$ (1)

$$P_{ion} + \alpha P_{cat} + k_{ab}(T_b - T_a) + k_{bp}(T_b - T_{prox}) + k_{sr}(T_b - T_{room}) = 0,$$ (2)

where

$$c_a = c_{a,0} + c_{a,1}T_a + c_{a,2}T_a^2,$$ (3)

$$k_{af} = k_{af,0} + k_{af,1}T_a + k_{af,2}T_a^2,$$ (4)

$$k_{ab} = k_{ab,0} + k_{ab,1}T_a + k_{ab,2}T_a^2,$$ (5)

$$k_{bp} = k_{bp,0} + k_{bp,1}T_b + k_{bp,2}T_b^2,$$ (6)

$$k_{br} = k_{br,0} + k_{br,1}T_b + k_{br,2}T_b^2,$$ (7)

$$\alpha = \alpha_0 + \alpha_1 T_b + \alpha_2 T_b^2.$$ (8)

Eq. 1 and 2 describe the heat flows within the model, while Eq. 3 through 8 expand each of the circuit elements into second order nonlinear parameters. Each of the conductances (k) and the capacitance (c), as well as a scaling factor that can be used if the sensitivity to P_{cat} is not the same as P_{ion}, are fitted during a calibration. In total, 18 parameters are needed to describe the model, although most of the time not all 18 parameters are used. Often many of the higher order terms are not needed to get a good fit.

v.   Fitting calibration results

To calibrate the calorimeter and validate the model, a set of samples were tested between 200 - 500 °C, a temperature at which BZCY is not expected to have any degradation issues. A set of current pulses and steps are used to stimulate each of the power source P_{RTD}, P_{cat}, and P_{ion}. Together with the measured temperatures from both the thermocouples and RTD, these power inputs are fed into a MATLAB script that uses the *nlgreyest* grey box estimator function, located

in the System Identification Toolbox™, to estimate the set of parameters θ that minimize the cost function:

$$V(\theta) = \frac{1}{t_{max}} \sum_{t=0}^{t_{max}} (\Delta T_{meas}(t) - \Delta T_{mod}(t, \theta))^2, \tag{9}$$

where

$$\Delta T_{meas}(t) = T_{prox}(t) - T_{a,meas}(t), \tag{10}$$

$$\Delta T_{mod}(t, \theta) = T_{prox}(t) - T_{a,mod}(t, \theta). \tag{11}$$

t is time ranging from 0 to t_{max}, the length of the experiment. The two temperatures in the cost function ΔT_{meas}, a measured temperature, and ΔT_{mod}, a modelled temperature, are differential measurements between the temperature at node a T_a (the temperature modelled or measured by the RTD) and the proximal thermocouple T_{prox}, which is always measured. This differential measurement allows for higher accuracy in the fitting process by presenting a small temperature range (a few °C) for the cost function to fit. Without taking this differential measurement, temperatures can fluctuate around 20 °C or more during fitting.

The fitting process is iterated until either the cost function is minimized below a cost tolerance or a maximum number of iterations in achieved. A goodness of fit is determined via the normalized root mean square error (NRMSE) of the difference between the measured temperature ΔT_{meas} and modelled temperature ΔT_{mod}. NRMSE values above 75% typically indicate a good fit.

An example calibration is shown in Figure 29. Input powers from each of the three sources, the measured temperatures, and the resulting fit compared to the measured data are plotted in succession. The NRMSE value of the fit in this case is 87%. The power inputs are designed with specific pulse lengths and pulse start times such that each power source can be separated from the other during analysis. By doing so, each source can be analyzed independently. The parameters that were obtained from the fitting are presented in Table IV. In this case only 9 out of the 16 possible parameters were used. Whether to go to first or second nonlinear parameters is dependent on the temperature range of the calibration. For small temperature ranges (<50 °C), only linear terms are often needed. However, as the temperature range increases to several hundred degrees, first order nonlinear terms need to be introduced. Beyond that second order terms may be needed, but they were not used in this study.
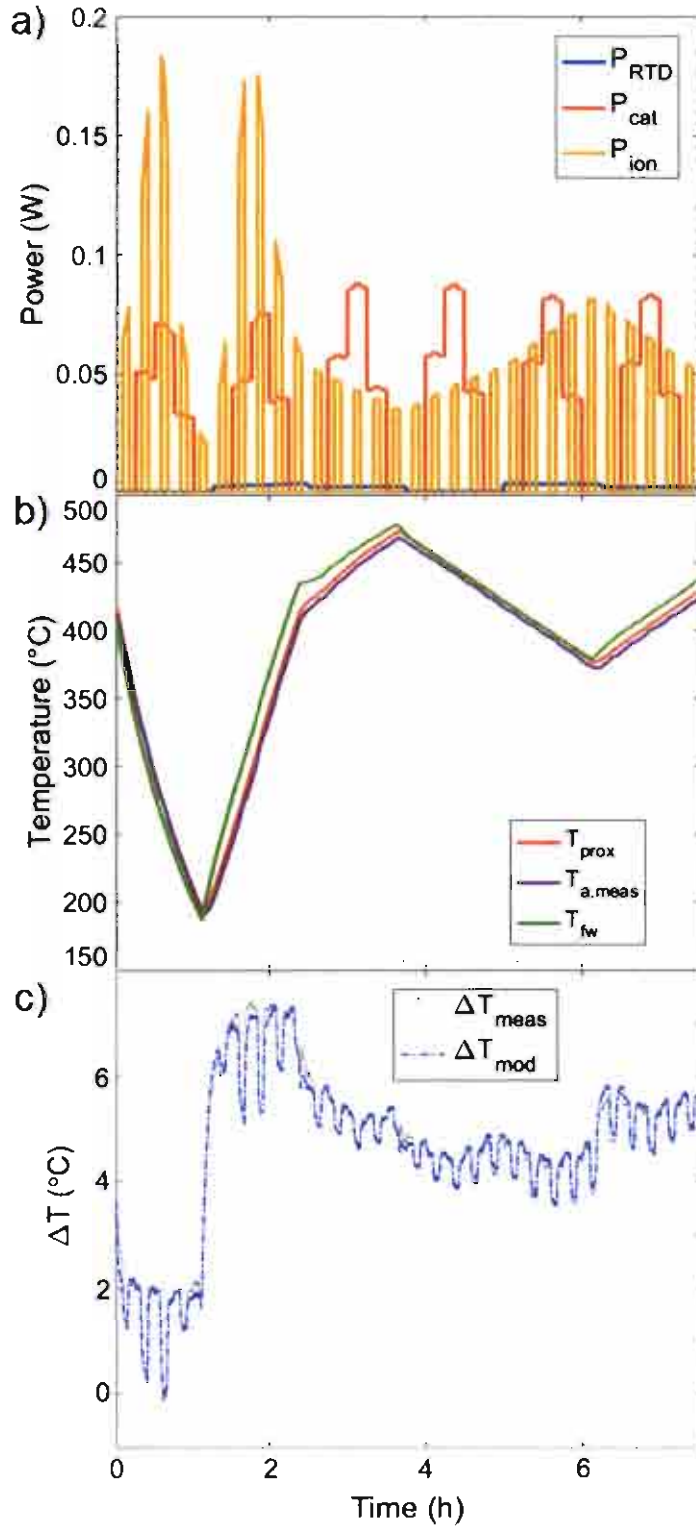
44

Figure 29. Calibration of the *in situ* calorimeter. (a) Input powers from three source P_{RTD}, P_{ion}, and P_{cat}. (b) Measured temperatures at the furnace wall T_{fw}, the proximal thermocouple T_{prox}, and

the RTD $T_{a,meas}$. (c) The differential temperature between T_{prox} and T_a for both measured node a temperature $T_{a,meas}$ and modelled node a temperature $T_{a,mod}$. The normalized root mean square error between the measured and modelled temperatures is 87%, indicating a good fit.

Table IV. Example model parameter values obtained from calibration

Parameter	Calibration Value
$c_{a,0}$	2.47E-1 J/K
$c_{a,1}$	-3.67E-3 J/K^2
$k_{ab,0}$	7.13E-2 W/K
$k_{ab,1}$	-8.98E-5 W/K^2
$k_{br,0}$	2.59E-3 W/K
$k_{br,1}$	-3.50E-6 W/K^2
$k_{bp,0}$	8.61E-2 W/K
$k_{bp,1}$	-7.52E-6 W/K^2
α	3.82E-1

vi.   Determining calorimeter sensitivity

After calibration, a second experiment in the same way as the calibration but with different power and temperature ranges and waveforms. This second step is called the prediction step. It is used to determine the sensitivity of the calorimeter to a new input, using the same parameters as in the calibration. An example prediction step is shown in Figure 30. Here, the power inputs have a waveform different than the one used to calibrate the calorimeter. In addition, the temperature profile is also varied. These changes in the inputs help to verify that the calorimeter model has not been overfitted to analyze only one particular type of dataset.
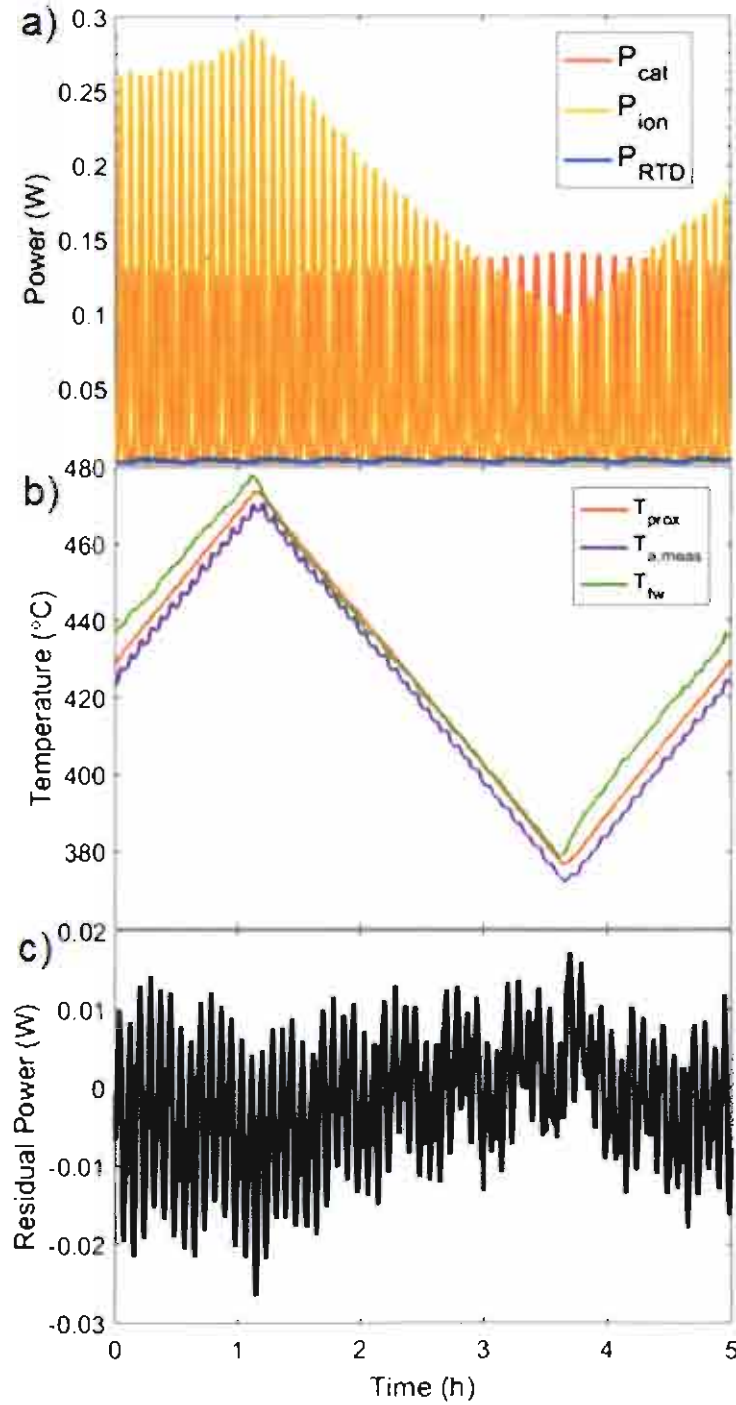
Figure 30. Prediction step used to determine calorimeter sensitivity. (a) The same three inputs are used as in the calibration but with different amplitudes and waveforms. (b) The temperature range is also changed to make sure that the calorimeter is not overfitting to a specific type of input. (c) The residual power, which is the difference between the power predicted by the model parameters given the measured temperatures and the actual power inputs, gives an idea of the

amount of noise present in the model. The standard deviation of the power residual here is 8.2 mW.

With parameters fixed from the calibration, the model is used to take the measured temperature data and predict what the power inputs should have been. The difference between this prediction and the actual power inputs is the residual power plotted in Figure 30c. By taking the standard deviation of this residual power, a sensitivity for the calorimeter can be determined. This value by itself is the related to the sensitivity of the calorimeter to P_{RTD} because power is at the node that is actually measured. An adjustment factor is introduced to determine the sensitivity of the other powers such as P_{ion} and P_{cat}. This adjustment factor can be found either through analysis of the equivalent circuit or by shutting off one of the powers during fitting and observing the change in residual power. Using the latter method (not shown), the adjustment factor was determined to be 2.6 for this dataset. The standard deviation is 8.2 mW from Figure 30c, so the adjusted standard deviation 21.3 mW. Any heat that exceeds two times this standard deviation, or 42.6 mW, can be detected with 95% certainty.

The calorimeter was tested over several samples to determine an average sensitivity. After performing calibration and prediction steps seven different samples, the sensitivity of the calorimeter was found to be 16.1 ± 11.7 mW, which meets the design objective set forth earlier and is far better than the example presented here. Although no degradation tests were actually made in this study, this calorimeter can be used in the future to run tests on solid oxide electrolytes to assess their performance and longevity during operation.

V.   Conclusion

There are three key takeaways in this study on the use of electrochemistry to insert H into Pd and the characterization of solid electrolytes:

(1) *In situ* XRD apparatuses were constructed that are capable of being used in a lab-scale X-ray powder diffractometer provide a means of quantifying H:Pd composition during electrochemical H insertion in an accurate and reproducible manner.

(2) The four parameters that appeared to improve the highest achievable H content in Pd are (a) thinner Pd cathodes, (b) lower temperatures, (c) use of liquid electrolytes, and (d) limiting electrochemomechanical damage.

(3) An *in situ* calorimeter was constructed to enable the study of high temperature solid oxide electrolytes while under operating conditions.

The information presented here can be used to further study the characteristics of Pd that promote H insertion, as well as the properties of solid oxide electrolytes, both of which are important for energy and electrocatalysis applications.

VI.   Acknowledgements

I would like to thank Dr. Yet-Ming Chiang for guidance and support throughout this project. This study could not have been completed without Drs. Ariel Jackson, Daniel Rettenwander, and Jesse Benck who worked with me as a team to plan and execute experiments, analyze data, and write up results, as well as always provided a welcoming and supportive environment to take on new challenges. I would like to acknowledge Matt Trevithick, Dr. David Fork, Dr. Ross Koningstein, and Seid Sadat, as well as the Burlinguette, Munday, and Yee groups at University of British Columbia, University of Maryland, and Georgia Institute of Technology, respectively, for informative discussions, great feedback, and assistance with data analysis. I would also like to acknowledge Dr. Charles Settens and Dr. Adam Phelan for their assistance and direction in performing diffraction experiments and crystal growth, respectively. Finally, I would like to thank family and friends for the encouragement and understanding, especially Kaiyue Chen who has been with me through thick and thin.

VII.   References

[1] Graham, T. (1866). On the Absorption and Dialytic Separation of Gases by Colloid Septa. *Philosophical Transactions 156*, 399-439.

[2] Hirose, K. (2010). *Handbook of hydrogen storage: new materials for future energy storage.* John Wiley & Sons.

[3] Cheon, Y. E., & Suh, M. P. (2009). Enhanced Hydrogen Storage by Palladium Nanoparticles Fabricated in a Redox-Active Metal–Organic Framework. *Angewandte Chemie International Edition, 48*(16), 2899-2903.

[4] Kishore, S., Nelson, J. A., Adair, J. H., & Eklund, P. C. (2005). Hydrogen storage in spherical and platelet palladium nanoparticles. *Journal of Alloys and Compounds, 389*(1-2), 234-242.

[5] Züttel, A. (2004). Hydrogen storage methods. *Naturwissenschaften, 91*(4), 157-172.

[6] Eberle, U., Felderhoff, M., & Schueth, F. (2009). Chemical and physical solutions for hydrogen storage. *Angewandte Chemie International Edition, 48*(36), 6608-6630.

[7] Adams, B. D., & Chen, A. (2011). The role of palladium in a hydrogen economy. *Materials Today, 14*(6), 282-289.

[8] Yun, S., & Oyama, S. T. (2011). Correlations in palladium membranes for hydrogen separation: a review. *Journal of Membrane Science, 375*(1-2), 28-45.

[9] Hatlevik, Ø., Gade, S. K., Keeling, M. K., Thoen, P. M., Davidson, A. P., & Way, J. D. (2010). Palladium and palladium alloy membranes for hydrogen separation and production: history, fabrication strategies, and current performance. *Separation and Purification Technology, 73*(1), 59-64.

[10] Nørskov, J. K., Bligaard, T., Logadottir, A., Bahn, S., Hansen, L. B., Bollinger, M., ... & Xu, Y. (2002). Universality in heterogeneous catalysis. *Journal of Catalysis, 209*(2), 275-278.

[11] Strasser, P., Koh, S., Anniyev, T., Greeley, J., More, K., Yu, C., ... & Toney, M. F. (2010). Lattice-strain control of the activity in dealloyed core–shell fuel cell catalysts. *Nature Chemistry, 2*(6), 454.

[12] Tang, W., Zhang, L., & Henkelman, G. (2011). Catalytic activity of Pd/Cu random alloy nanoparticles for oxygen reduction. *The Journal of Physical Chemistry Letters, 2*(11), 1328-1331.

[13] Errea, I., Calandra, M., & Mauri, F. (2013). First-principles theory of anharmonicity and the inverse isotope effect in superconducting palladium-hydride compounds. *Physical Review Letters, 111*(17), 177002.

[14] Harper, J. M. E. (1974). Effect of hydrogen concentration on superconductivity and clustering in palladium hydride. *Physics Letters A, 47*(1), 69-70.

[15] Skoskiewicz, T., Szafranski, A. W., Bujnowski, W., & Baranowski, B. (1974). Isotope effect in the superconducting palladium-hydrogen-deuterium system. *Journal of Physics C: Solid State Physics*, *7*(15), 2670.

[16] Wilde, B. E., Chattoraj, I., & Mozhi, T. A. (1987). The influence of palladium on the resistance of low alloy steels to hydrogen embrittlement. *Scripta Metallurgica*, *21*(10), 1369-1373.

[17] Balbaa, I. S., Hardy, P. A., San-Martin, A., Coulter, P. G., & Machester, F. D. (1987). The effect of lattice distortions on the X-ray measurement of lattice parameters for PdH_x. I. Empirical relationships. *Journal of Physics F: Metal Physics*, *17*(10), 2041.

[18] Schirber, J. E., & Morosin, B. (1975). Lattice constants of $\beta - PdH_x$ and $\beta - PdD_x$ with x near 1.0. *Physical Review B*, *12*(1), 117.

[19] Maeland, A., & Flanagan, T. B. (1964). Lattice Constants and Thermodynamic Parameters of the Hydrogen—Platinum—Palladium and Deuterium—Platinum—Palladium Systems. *The Journal of Physical Chemistry*, *68*(6), 1419-1426.

[20] Wicke, V. E. & Nernst, G. H. (1964). Zustandsdiagramm und thermodynamisches Verhalten der Systeme Pd/H_2 und Pd/D_2 bei normalen Temperaturen; H/D-Trenneffekte. *Berichte der Bunsengesellschaft*, *60*(3), 224-235.

[21] Manchester, F. D., San-Martin, A., & Pitre, J. M. (1994). The H-Pd (hydrogen-palladium) system. *Journal of Phase Equilibria*, *15*(1), 62-83.

[22] Mahato, N., Banerjee, A., Gupta, A., Omar, S., & Balani, K. (2015). Progress in material selection for solid oxide fuel cell technology: A review. *Progress in Materials Science*, *72*, 141-337.

[23] Steele, B. C., & Heinzel, A. (2011). Materials for fuel-cell technologies. In *Materials For Sustainable Energy: A Collection of Peer-Reviewed Research and Review Articles from Nature Publishing Group* (pp. 224-231).

[24] Mauritz, K. A., & Moore, R. B. (2004). State of understanding of Nafion. *Chemical Reviews*, *104*(10), 4535-4586.

[25] Lewis, N. S., Barnes, C. A., Heben, M. J., Kumar, A., Lunt, S. R., McManis, G. E., ... & Shreve, G. A. (1989). Searches for low-temperature nuclear fusion of deuterium in palladium. *Nature*, *340*(6234), 525.

[26] Czerwiński, A., Kiersztyn, I., Grdeń, M., & Czapla, J. (1999). The study of hydrogen sorption in palladium limited volume electrodes (Pd-LVE): I. Acidic solutions. *Journal of Electroanalytical Chemistry*, *471*(2), 190-195.

[27] Łukaszewski, M., & Czerwiński, A. (2006). Electrochemical quartz crystal microbalance study on hydrogen absorption and desorption into/from palladium and palladium–noble metal alloys. *Journal of Electroanalytical Chemistry*, *589*(1), 87-95.

[28] Zhang, W. S., Zhang, Z. F., & Zhang, Z. L. (2002). Some problems on the resistance method in the in situ measurement of hydrogen content in palladium electrode. *Journal of Electroanalytical Chemistry, 528*(1-2), 1-17.

[29] Felici, R., Bertalot, L., DeNinno, A., LaBarbera, A., & Violante, V. (1995). In situ measurement of the deuterium (hydrogen) charging of a palladium electrode during electrolysis by energy dispersive x-ray diffraction. *Review of Scientific Instruments, 66*(5), 3344-3348.

[30] Knies, D. L., Violante, V., Grabowski, K. S., Hu, J. Z., Dominguez, D. D., He, J. H., ... & Hubler, G. K. (2012). In-situ synchrotron energy-dispersive x-ray diffraction study of thin Pd foils with Pd:D and Pd:H concentrations up to 1:1. *Journal of Applied Physics, 112*(8), 083510.

[31] Fukada, Y., Hioki, T., Motohiro, T., & Ohshima, S. (2015). In situ x-ray diffraction study of crystal structure of Pd during hydrogen isotope loading by solid-state electrolysis at moderate temperatures 250– 300° C. *Journal of Alloys and Compounds, 647*, 221-230.

[32] Fukada, Y., Hioki, T., & Motohiro, T. (2016). Multiple phase separation of super-abundant-vacancies in Pd hydrides by all solid-state electrolysis in moderate temperatures around 300° C. *Journal of Alloys and Compounds, 688*, 404-412.

[33] Siebel, A., Gorlin, Y., Durst, J., Proux, O., Hasché, F., Tromp, M., & Gasteiger, H. A. (2016). Identification of Catalyst Structure during the Hydrogen Oxidation Reaction in an Operating PEM Fuel Cell. *ACS Catalysis, 6*(11), 7326-7334.

[34] Fukai, Y., & Ōkuma, N. (1993). Evidence of copious vacancy formation in Ni and Pd under a high hydrogen pressure. *Japanese Journal of Applied Physics, 32*(9A), L1256.

[35] Fukai, Y., & Ōkuma, N. (1994). Formation of superabundant vacancies in Pd hydride under high hydrogen pressures. *Physical Review Letters, 73*(12), 1640.

[36] Brownsberger, K., Ahart, M., Somayazulu, M., Park, C., Gramsch, S. A., & Hemley, R. J. (2017). X-ray Diffraction, Lattice Structure, and Equation of State of PdH x and PdD x to Megabar Pressures. *The Journal of Physical Chemistry C, 121*(49), 27327-27331.

[37] Hemmes, H., Geerken, B. M., & Griessen, R. (1984). Contribution of optical phonons to the thermal expansion of α'-PdH$_x$ and α'-PdD$_x$. *Journal of Physics F: Metal Physics, 14*(12), 2923.

[38] Dutta, B. N., & Dayal, B. (1963). Lattice Constants and Thermal Expansion of Palladium and Tungsten up to 878° C by X-Ray Method. *Physica Status Solidi (b), 3*(12), 2253-2259.

[39] Eastman, J. A., Thompson, L. J., & Kestel, B. J. (1993). Narrowing of the palladium-hydrogen miscibility gap in nanocrystalline palladium. *Physical Review B, 48*(1), 84.

[40] Seymour, E. F. W., Cotts, R. M., & Williams, W. D. (1975). NMR measurement of hydrogen diffusion in β-palladium hydride. *Physical Review Letters, 35*(3), 165.

[41] Mahato, N., Banerjee, A., Gupta, A., Omar, S., & Balani, K. (2015). Progress in material selection for solid oxide fuel cell technology: A review. *Progress in Materials Science, 72*, 141-337.

[42] Laguna-Bercero, M. A. (2012). Recent advances in high temperature electrolysis using solid oxide fuel cells: A review. *Journal of Power Sources, 203*, 4-16.

[43] Ebbesen, S. D., & Mogensen, M. (2009). Electrolysis of carbon dioxide in solid oxide electrolysis cells. *Journal of Power Sources, 193*(1), 349-358.

[44] Downie, L. E., & Dahn, J. R.m (2014). Determination of the voltage dependence of parasitic heat flow in lithium ion cells using isothermal microcalorimetry. *Journal of The Electrochemical Society, 161*(12), A1782-A1787.

[45] Glazier, S. L., Downie, L. E., Xia, J., Louli, A. J., & Dahn, J. R. (2016). Effects of fluorinated carbonate solvent blends on high voltage parasitic reactions in lithium ion cells using OCV isothermal microcalorimetry. *Journal of The Electrochemical Society, 163*(10), A2131-A2138.

[46] Saito, Y., Shikano, M., & Kobayashi, H. (2013). Heat generation behavior during charging and discharging of lithium-ion batteries after long-time storage. *Journal of Power Sources, 244*, 294-299.

[47] Zuo, C., Zha, S., Liu, M., Hatano, M., & Uchiyama, M. (2006). Ba (Zr0. 1Ce0. 7Y0. 2) O3–δ as an electrolyte for low-temperature solid-oxide fuel cells. *Advanced Materials, 18*(24), 3318-3320.

[48] Fabbri, E., Bi, L., Pergolesi, D., & Traversa, E. (2012). Towards the Next Generation of Solid Oxide Fuel Cells Operating Below 600° C with Chemically Stable Proton-Conducting Electrolytes. *Advanced materials, 24*(2), 195-208.

[49] van Duin, A. C., Merinov, B. V., Han, S. S., Dorso, C. O., & Goddard Iii, W. A. (2008). ReaxFF reactive force field for the Y-doped $BaZrO_3$ proton conductor with applications to diffusion rates for multigranular systems. *The Journal of Physical Chemistry A, 112*(45), 11414-11422.

[50] Yang, J. H., Kim, B. K., & Kim, Y. C. (2015). Calculation of proton conductivity at the Σ3 (111)/[$\overline{1}1\overline{0}$] tilt grain boundary of barium zirconate using density functional theory. *Solid State Ionics, 279*, 60-65.

[51] Iguchi, F., Tsurui, T., Sata, N., Nagao, Y., & Yugami, H. (2009). The relationship between chemical composition distributions and specific grain boundary conductivity in Y-doped $BaZrO_3$ proton conductors. *Solid State Ionics, 180*(6-8), 563-568.

[52] Iguchi, F., Sata, N., Tsurui, T., & Yugami, H. (2007). Microstructures and grain boundary conductivity of $BaZr_{1-x}Y_xO_3$ (x= 0.05, 0.10, 0.15) ceramics. *Solid State Ionics, 178*(7-10), 691-695.

[53] Kjølseth, C., Fjeld, H., Prytz, Ø., Dahl, P. I., Estournès, C., Haugsrud, R., & Norby, T. (2010). Space–charge theory applied to the grain boundary impedance of proton conducting $BaZr_{0.9}Y_{0.1}O_{3-\delta}$. *Solid State Ionics, 181*(5-7), 268-275.

[54] Pergolesi, D., Fabbri, E., D'Epifanio, A., Di Bartolomeo, E., Tebano, A., Sanna, S., ... & Traversa, E. (2010). High proton conduction in grain-boundary-free yttrium-doped barium zirconate films grown by pulsed laser deposition. *Nature Materials*, *9*(10), 846.

[55] Shevchenko, A. V., Lopato, L. M., Gerasimyuk, G. I., & Zajtseva, Z. A. (1987). Reaction in the systems HfO_2-SrO, HfO_2-BaO and ZrO_2-BaO in the regions with a high content of HfO_2 (ZrO_2). *Izvestiya Akademii Nauk SSSR*, *23*(9), 1495-1499.

[56] Guillaume, B., Boschini, F., Garcia-Cano, I., Rulmont, A., Cloots, R., & Ausloos, M. (2005). Optimization of $BaZrO_3$ sintering by control of the initial powder size distribution; a factorial design statistical analysis. *Journal of the European Ceramic Society*, *25*(16), 3593-3604.

[57] Yan, N., Zeng, Y., Shalchi, B., Wang, W., Gao, T., Rothenberg, G., & Luo, J. L. (2015). Discovery and understanding of the ambient-condition degradation of doped barium cerate proton-conducting perovskite oxide in solid oxide fuel cells. *Journal of The Electrochemical Society*, *162*(14), F1408-F1414.

[58] Boysen, D. A., Uda, T., Chisholm, C. R., & Haile, S. M. (2004). High-performance solid acid fuel cells through humidity stabilization. *Science*, *303*(5654), 68-70.

[59] Chervin, C., Glass, R. S., & Kauzlarich, S. M. (2005). Chemical degradation of $La_{1-x}Sr_xMnO_3$/Y_2O_3-stabilized ZrO_2 composite cathodes in the presence of current collector pastes. *Solid State Ionics*, *176*(1-2), 17-23.

[60] Lufrano, F., Gatto, I., Staiti, P., Antonucci, V., & Passalacqua, E. (2001). Sulfonated polysulfone ionomer membranes for fuel cells. *Solid State Ionics*, *145*(1-4), 47-51.

[61] Wachsman, E. D., & Lee, K. T. (2011). Lowering the temperature of solid oxide fuel cells. *Science*, *334*(6058), 935-939.

[62] Sharaf, O. Z., & Orhan, M. F. (2014). An overview of fuel cell technology: Fundamentals and applications. *Renewable and Sustainable Energy Reviews*, *32*, 810-853.

[63] Chervin, C., Glass, R. S., & Kauzlarich, S. M. (2005). Chemical degradation of $La_{1-x}Sr_xMnO_3$/Y_2O_3-stabilized ZrO_2 composite cathodes in the presence of current collector pastes. *Solid State Ionics*, *176*(1-2), 17-23.